

The clustering of galaxies in the SDSS-III Baryon Oscillation Spectroscopic Survey: RSD measurement from the LOS-dependent power spectrum of DR12 BOSS galaxies

Héctor Gil-Marín^{1*}, Will J. Percival¹, Joel R. Brownstein², Chia-Hsun Chuang³, Jan Niklas Grieb^{4,5}, Shirley Ho⁶, Francisco-Shu Kitaura⁷, Claudia Maraston¹, Francisco Prada^{3,8,9}, Sergio Rodríguez-Torres^{3,10,8}, Ashley J. Ross¹¹, Lado Samushia^{12,13}, David J. Schlegel¹⁴, Daniel Thomas¹, Jeremy L. Tinker¹⁵ & Gong-Bo Zhao^{1,16}

¹ *Institute of Cosmology & Gravitation, University of Portsmouth, Dennis Sciama Building, Portsmouth PO1 3FX, UK*

² *Department of Physics and Astronomy, University of Utah, 115 S 1400 E, Salt Lake City, UT 84112, USA*

³ *Instituto de Física Teórica, (UAM/CSIC), Universidad Autónoma de Madrid, Cantoblanco, E-28049 Madrid, Spain*

⁴ *Universitäts-Sternwarte München, Ludwig-Maximilians-Universität München, Scheinerstraße 1, 81679 München, Germany*

⁵ *Max-Planck-Institut für extraterrestrische Physik, Postfach 1312, Giessenbachstr., 85741 Garching, Germany*

⁶ *McWilliams Center, Carnegie Mellon University, Pittsburgh, PA 15213, USA*

⁷ *Leibniz-Institut für Astrophysik (AIP), An der Sternwarte 16, D-14482 Potsdam, Germany*

⁸ *Departamento de Física Teórica, Universidad Autónoma de Madrid, Cantoblanco, 28049, Madrid, Spain*

⁹ *Instituto de Astrofísica de Andalucía (CSIC), Glorieta de la Astronomía, E-18080 Granada, Spain*

¹⁰ *Campus of International Excellence UAM+CSIC, Cantoblanco, E-28049 Madrid, Spain*

¹¹ *Center for Cosmology and AstroParticle Physics, The Ohio State University, Columbus, OH 43210, USA*

¹² *Department of Physics, Kansas State University, 116, Cardwell Hall, Manhattan, KS, 66506, USA*

¹³ *National Abastumani Astrophysical Observatory, Iliia State University, 2A Kazbegi Ave., GE-1060 Tbilisi, Georgia*

¹⁴ *Lawrence Berkeley National Lab 1 Cyclotron Road, Berkeley, CA 94720 USA*

¹⁵ *Center for Cosmology and Particle Physics, Department of Physics, New York University, New York, NY 10003, USA*

¹⁶ *National Astronomy Observatories, Chinese Academy of Science, Beijing, 100012, P. R. China*

30 May 2016

ABSTRACT

We measure and analyse the clustering of the Baryon Oscillation Spectroscopic Survey (BOSS) relative to the line-of-sight (LOS), for LOWZ and CMASS galaxy samples drawn from the final Data Release 12 (DR12). The LOWZ sample contains 361 762 galaxies with an effective redshift of $z_{\text{lowz}} = 0.32$, and the CMASS sample 777 202 galaxies with an effective redshift of $z_{\text{cmass}} = 0.57$. From the power spectrum monopole and quadrupole moments around the LOS, we measure the growth of structure parameter f times the amplitude of dark matter density fluctuations σ_8 by modeling the Redshift-Space Distortion signal. When the geometrical Alcock-Paczynski effect is also constrained from the same data, we find joint constraints on $f\sigma_8$, the product of the Hubble constant and the comoving sound horizon at the baryon drag epoch $H(z)r_s(z_d)$, and the angular distance parameter divided by the sound horizon $D_A(z)/r_s(z_d)$. We find $f(z_{\text{lowz}})\sigma_8(z_{\text{lowz}}) = 0.394 \pm 0.062$, $D_A(z_{\text{lowz}})/r_s(z_d) = 6.35 \pm 0.19$, $H(z_{\text{lowz}})r_s(z_d) = (11.41 \pm 0.56) 10^3 \text{kms}^{-1}$ for the LOWZ sample, and $f(z_{\text{cmass}})\sigma_8(z_{\text{cmass}}) = 0.444 \pm 0.038$, $D_A(z_{\text{cmass}})/r_s(z_d) = 9.42 \pm 0.15$, $H(z_{\text{cmass}})r_s(z_d) = (13.92 \pm 0.44) 10^3 \text{kms}^{-1}$ for the CMASS sample. We find general agreement with previous BOSS DR11 measurements. Assuming the Hubble parameter and angular distance parameter are fixed at fiducial Λ CDM values, we find $f(z_{\text{lowz}})\sigma_8(z_{\text{lowz}}) = 0.485 \pm 0.044$ and $f(z_{\text{cmass}})\sigma_8(z_{\text{cmass}}) = 0.436 \pm 0.022$ for the LOWZ and CMASS samples, respectively.

Key words: cosmology: theory - cosmology: cosmological parameters - cosmology: large-scale structure of Universe - galaxies: haloes

1 INTRODUCTION

The large-scale distribution of matter, as observed through galaxy clustering, encodes significant cosmological information. Much of this can be extracted from the shape and amplitude of the galaxy power spectrum multipole moments. The focus of this paper is the observed anisotropic redshift-space distortions (RSD; Kaiser 1987) caused by peculiar velocities, which contain information about how gravity behaves at large scales and about the total matter content of the Universe. As these distortions depend on the growth of structure, they offer an independent and complementary technique to measure the matter content and to test gravity, compared to studies of the cosmic expansion history.

In this paper we measure the galaxy power spectrum monopole and quadrupole moments calculated from the galaxy sample of the Sloan Digital Sky Survey III (Eisenstein et al. 2011) Baryon Oscillation Spectroscopic Survey (BOSS; Bolton et al. 2012; Dawson et al. 2013; Smee et al. 2013) data release 12 (DR12; Alam et al. 2015a). The galaxy catalogues drawn from the final data release from BOSS, DR12, cover the largest cosmic volume ever observed, with an effective volume $V_{\text{eff}} = 7.4 \text{ Gpc}^3$ (Reid et al. 2015). The number of independent modes contained allows us to observe the RSD with the highest ever significance, and use them to set tight constraints on the growth of structure f times the amplitude of primordial dark matter power spectrum σ_8 at the effective redshifts of $z = 0.32$ and $z = 0.57$. Additionally we are able to constrain $D_A(z_{\text{eff}})/r_s(z_d)$ and $H(z_{\text{eff}})r_s(z_d)$ by performing the Alcock-Paczynski test (AP; Alcock & Paczynski 1979).

This paper forms part of an initial set of DR12 papers produced by the BOSS galaxy clustering team. In (Cuesta et al. 2015, companion paper) we measure BAO from the correlation function moments measuring the cosmological expansion history. A complimentary approach is provided in (Gil-Marín et al. 2015b, companion paper), which looks at the Baryon Acoustic Oscillation (BAO) in power spectrum monopole and quadrupole moments, with both papers applying an algorithm to reconstruct the primordial density distribution. The BOSS galaxy targeting and catalogue creation algorithms are presented in Reid et al. (2015), which includes an extensive analysis of the catalogues themselves, and the methods employed to correct for observational effects.

RSD measurements have a long history following the seminal theoretical paper of Kaiser (1987), and the development of large galaxy surveys. Key milestones include measurements from the PSCz galaxy survey (Tadros et al. 1999), 2-degree Field Galaxy Redshift Survey (Peacock et al. 2001; Hawkins et al. 2003; Percival et al. 2004), WiggleZ (Blake et al. 2012), 6-degree Field Galaxy Survey (Beutler et al. 2012) and the SDSS-II LRGs (Oka et al. 2014). Previous measurements made from BOSS including DR9, when the survey was approximately one third complete (Samushia et al. 2013), and most recently from DR10/11 (Chuang et al. 2013; Beutler et al. 2014; Samushia et al. 2014; Sánchez et al. 2014; Reid et al. 2014; Alam et al. 2015b).

The RSD measurements made from the BOSS DR11 sample, which are discussed further in §7, exhibit a scatter that is not negligible with respect to the statistical errors. This is caused by adopting different approaches to model

quasi-linear and non-linear behaviour in the measured clustering, beyond the linear RSD signal. As the signal-to-noise increases as we move to small scales, RSD measurements are very sensitive to the behaviour of the model on the smallest scales fitted. It is therefore important that the model is general enough to encompass all of the unknown behaviour, whilst also being able to accurately model the data itself. Consequently, a large effort on developing a model that is able to account for: i) mode-coupling; ii) galaxy bias; iii) RSD ; up to quasi- and non-linear scales is required. Some improvements have recently been achieved on i) beyond the linear regime for the real space power spectrum using perturbation theory schemes. There are several models that attempt to do this task: cosmological standard perturbation theory (see Bernardeau et al. 2002 and references therein), Lagrangian perturbation theories (Hivon et al. 1995; Matsubara 2008; Carlson, White & Padmanabhan 2009; Okamura, Taruya & Matsubara 2011; Valageas & Nishimichi 2011), time renormalization (Pietroni 2008; Anselmi & Pietroni 2012), Eulerian resummed perturbation theories (Crocce & Scoccimarro 2006; Bernardeau, Crocce & Scoccimarro 2008; Wang & Szalay 2012; Elia et al. 2011; Taruya et al. 2012; Bernardeau, Crocce & Scoccimarro 2012) and closure theory (Taruya & Hiramatsu 2008). Recent improvements in the galaxy bias model describe accurately how the galaxies trace dark matter, including non-linear and non-local terms (Nishimichi & Taruya 2011; McDonald & Roy 2009; Saito et al. 2014) in addition to primordial non-Gaussian terms (Biagetti et al. 2014). The final point iii) is to accurately model the mapping from real to redshift space statistics. Different approaches to this problem includes: the TNS model (Taruya, Nishimichi & Saito 2010), the Distribution function approach model (Vlah et al. 2012; Okumura, Seljak & Desjacques 2012) and the Gaussian streaming model (Reid & White 2011).

In this paper we use a resummed perturbation theory approach (RPT) in order to describe the dark matter non-linear power spectra components as it is described in Gil-Marín et al. (2012). We combine this approach with the non-linear and non-local galaxy bias model of McDonald & Roy (2009), as it was done in previous analyses (Beutler et al. 2014; Gil-Marín et al. 2015a). Finally, we account for the RSD using the redshift space mapping presented in Taruya, Nishimichi & Saito (2010); Nishimichi & Taruya (2011). This modelling has demonstrated to describe accurately the RSD for both dark matter particles and dark matter haloes (Gil-Marín et al. 2012, 2014). Note that in previous approaches, Beutler et al. (2014) use a different model of RPT to describe the dark matter components and a different k -range is considered for obtaining the best-fit parameters. Also in this paper we treat f and σ_8 as a free independent parameters during the fitting process, and is only at the end of the analysis which we constrain $f\sigma_8$. On the other hand Beutler et al. (2014) constrain $f\sigma_8$ fixing the value of σ_8 on the non-linear components of the model, which do not depend on the particular combination $f \times \sigma_8$.

This paper is organised as follows. In §2 we present the description of the LOWZ and CMASS DR12 data samples and the resources used for computing the covariance matrices and for testing the theoretical models. In §3 we present the estimator used for measuring the power spectrum multipoles. In §4 the results including the best-fit parameters and

their errors are presented. §5 contains information about the theoretical models used to describe the galaxy power spectrum multipoles in redshift space. In this section, we also include information about how to model the AP distortions and the effect of the survey window in the measurements. In §6 we present the details about the parameter estimation, including how the covariance matrices are extracted and how the best-fit parameters and their errors have been computed. In §7 we present a final analysis of the results presented in §4 and how they compare with other galaxy surveys and other BOSS analyses, as well as the effect that changing the cosmological model has on $f\sigma_8$. Finally, in §8 we present the conclusions of this paper.

2 DATA AND MOCKS

2.1 The SDSS III BOSS data

As part of the Sloan Digital Sky Survey III (Eisenstein et al. 2011) the Baryon Oscillations Spectroscopic Survey (BOSS) (Dawson et al. 2013) measured spectroscopic redshifts for more than 1 million galaxies and over 200 000 quasars. The galaxies were selected from multi-colour SDSS imaging (Fukugita et al. 1996; Gunn et al. 1998; Smith et al. 2002; Gunn et al. 2006; Doi et al. 2010) focussing on the redshift range of $0.15 \leq z \leq 0.70$. The galaxy survey used two primary target algorithms, selecting samples called LOWZ, with 361 762 galaxies in the final data release DR12 (Alam et al. 2015a) between $0.15 \leq z \leq 0.43$ and CMASS, with 777 202 galaxies in DR12 between $0.43 \leq z \leq 0.70$. The full targeting algorithms used and the method for calculating the galaxy and random catalogues are presented in Reid et al. (2015), which also shows that the samples jointly cover a large cosmic volume $V_{\text{eff}} = 7.4 \text{ Gpc}^3$ with a number density of galaxies as a function of observed redshift, that ensures that the shot noise does not dominate at BAO scales. Full details of the catalogues are provided in Reid et al. (2015), and we do not replicate this here.

In order to correct for several observational artifacts in the catalogues, the CMASS and LOWZ samples incorporate weights: a redshift failure weight, w_{rf} , a fibre collision weight, w_{fc} , and a systematic weight, w_{sys} (CMASS only), which combines a seeing condition weight and a stellar weight (Ross et al. 2012; Anderson et al. 2014; Reid et al. 2015). Hence, each galaxy target contributes to our estimate of the target galaxy density field by

$$w_c = w_{\text{sys}}(w_{\text{rf}} + w_{\text{fc}} - 1). \quad (1)$$

The redshift failure weights account for galaxies that have been observed, but whose redshifts have not been measured: nearby galaxies, which are approximated as being “equivalent” are up-weighted to remove any bias in the resulting field. The fibre collision weight similarly corrects for galaxies that could not be observed as there was another target within $62''$, a physical limitation of the spectrograph (see Ross et al. (2012) for details). The systematic weight accounts for fluctuations in the target density caused by changes in the observational efficiency. It is only present for the CMASS sample, which relies on deeper imaging data, and such a weight is not required for the brighter LOWZ sample.

Additionally, we use the standard weight to balance regions of high and low density (Feldman, Kaiser & Peacock 1994; Beutler et al. 2014),

$$w_{\text{FKP}}(\mathbf{r}) = \frac{w_{\text{sys}}(\mathbf{r})}{w_{\text{sys}}(\mathbf{r}) + w_c(\mathbf{r})n(\mathbf{r})P_{\text{bao}}}, \quad (2)$$

where n is the mean number density of galaxies and P_{bao} is the amplitude of the galaxy power spectrum at the scale where the error is minimised. We assume $P_{\text{bao}} = 10\,000 \text{ Mpc}^3 h^{-3}$, which corresponds to the amplitude of the power spectrum at scales $k \sim 0.10 \text{ hMpc}^{-1}$ (Reid et al. 2015).

2.2 The mock survey catalogues

Galaxy mock catalogues have become an essential tool in the analysis of precision cosmological data provided by galaxy surveys. They provide a fundamental test of large-scale structure analyses and help to determine errors on measurements. As much of the large-scale physics can be captured using approximate methods, we do not necessarily need to base mock catalogues on full N-body cosmological simulations: structure formation models can be calibrated with a small number of N-body simulations, and the parameter space studied using a more efficient scheme. In this paper we use mocks created by two different approaches: MultiDark-Patchy BOSS DR12 mocks¹ (hereafter MD-PATCHY) (Kitaura et al. 2015, companion paper) and Quick-Particle-Mesh mocks (hereafter QPM) (White, Tinker & McBride 2014). Both schemes incorporate observational effects including the survey selection window, veto mask and fiber collisions.

MD-PATCHY mocks rely on Augmented Lagrangian Perturbation Theory (ALPT) formalism (Kitaura & Heß 2013), which is based on splitting the displacement field into a long and a short-range component. The long-range component is computed by second order Lagrangian Perturbation Theory (2LPT), whereas the short-range component is modeled using the spherical collapse approximation. The MD-PATCHY mocks use 10 combined snapshots at $z = 0.1885, 0.2702, 0.3153, 0.3581, 0.3922, 0.4656, 0.5053, 0.5328, 0.5763, 0.6383$. The underlying cosmology for these mocks has been chosen to be $(\Omega_\Lambda, \Omega_m, \Omega_b, \sigma_8, h, n_s) = (0.692885, 0.307115, 0.048, 0.8288, 0.6777, 0.96)$, being very close to the best-fit values of the last release of *Planck15* (Planck Collaboration et al. 2015). For this cosmological model the sound horizon at the baryon-drag redshift is $r_s(z_d) = 147.66 \text{ Mpc}$.

The QPM mocks are based on low-resolution particle mesh simulations that accurately reproduce the large-scale dark matter density field, in combination with the halo occupation distribution technique (HOD) to populate the resolved haloes with galaxies. For the QPM mocks, the snapshots are at the effective redshift of, $z_{\text{eff}} = 0.55$ for CMASS and $z_{\text{eff}} = 0.40$ for LOWZ. The underlying cosmology for these mocks has been chosen to be $(\Omega_\Lambda, \Omega_m, \Omega_b, \sigma_8, h, n_s) = (0.71, 0.29, 0.0458, 0.80, 0.7, 0.97)$. For this cosmological

¹ <http://data.sdss3.org/datamodel/index-files.html>

model the sound horizon at the baryon-drag redshift is $r_s(z_d) = 147.10$ Mpc.

2.3 Fiducial Cosmology

We have opted to analyse both mocks and data using the same cosmological model. The fiducial value assumed for this is $\Omega_m^{\text{fid}} = 0.31$, which is in agreement with the last *Planck15* release. As a consequence we will analyse the mocks using a value of Ω_m that is different than their true values. When converting redshift into comoving distances, this will introduce an extra anisotropy to the one generated by the peculiar velocities. In our analysis this effect will be accounted by the AP scaling relations presented in §5.3. The rest of cosmological parameters in the fiducial cosmology are $\mathbf{\Omega}^{\text{fid}} \equiv (\Omega_\Lambda^{\text{fid}}, \Omega_m^{\text{fid}}, \Omega_b^{\text{fid}}, \sigma_8^{\text{fid}}, h^{\text{fid}}, n_s^{\text{fid}}) = (0.69, 0.31, 0.049, 0.8475, 0.6711, 0.9624)$. For this cosmology the sound horizon at the baryon-drag redshift is $r_s(z_d) = 148.11$ Mpc.

3 MEASURING POWER SPECTRUM MOMENTS

In order to compute the galaxy power spectrum we start by defining the Feldman-Kaiser-Peacock function (Feldman, Kaiser & Peacock 1994),

$$F(\mathbf{r}) = \frac{w_{\text{FKP}}(\mathbf{r})}{I_2^{1/2}} [w_c(\mathbf{r})n(\mathbf{r}) - \alpha n_s(\mathbf{r})], \quad (3)$$

where n and n_s are, respectively, the observed number density of galaxies and the number density of a synthetic catalog Poisson sampled with the same mask and selection function as the survey with no other cosmological correlations. The functions w_c and w_{FKP} were defined in Eqs 1 and 2 respectively. The factor α is the ratio between the weighted number of observed galaxies over the random catalogue, $\alpha \equiv \sum_i^{N_{\text{gal}}} w_c / N_s$, where N_s denotes the number of objects in the synthetic catalog and N_{gal} the number of galaxies in the real catalog. The factor I_2 normalises the amplitude of the observed power in accordance with its definition in a universe with no survey selection,

$$I_2 \equiv \int d^3\mathbf{r} w_{\text{FKP}}^2 \langle n w_c \rangle^2(\mathbf{r}). \quad (4)$$

Following the Yamamoto estimator (Yamamoto et al. 2006), we define the multipole power spectrum estimator as,

$$\begin{aligned} \hat{P}_{\text{Yama}}^{(\ell)}(k) &= \frac{(2\ell + 1)}{I_2} \int \frac{d\Omega_k}{4\pi} \left[\int d\mathbf{r}_1 F(\mathbf{r}_1) e^{i\mathbf{k}\cdot\mathbf{r}_1} \right. \\ &\quad \times \left. \int d\mathbf{r}_2 F(\mathbf{r}_2) e^{-i\mathbf{k}\cdot\mathbf{r}_2} \mathcal{L}_\ell(\hat{\mathbf{k}} \cdot \hat{\mathbf{r}}_2) - P_{\text{Poisson}}^{(\ell)}(\mathbf{k}) \right], \end{aligned} \quad (5)$$

where $d\Omega_k$ is the solid angle element, \mathcal{L}_ℓ is the Legendre polynomial of order ℓ , $P_{\text{Poisson}}^{(\ell)}$ is the Poisson shot noise term,

$$P_{\text{Poisson}}^{(\ell)}(\mathbf{k}) = (1 + \alpha) \int d\mathbf{r} \bar{n}(\mathbf{r}) w^2(\mathbf{r}) \mathcal{L}_\ell(\hat{\mathbf{k}} \cdot \hat{\mathbf{r}}), \quad (6)$$

where the integral has been performed as a sum over the galaxy catalogue. For multipoles of order $\ell > 0$, $P_{\text{Poisson}}^{(\ell)} \ll \hat{P}^{(\ell)}$, and consequently the shot noise correction is negligible. This estimator keeps the relevant LOS information by

approximating the LOS of each pair of galaxies with the LOS of one of the two galaxies. This is a reliable approximation on the scales of interest, which clearly improves on assuming a single fixed LOS for the whole survey for $l > 0$, but will eventually break down at very large scales and high order multipoles (Yoo & Seljak 2015; Samushia, Branchini & Percival 2015).

The implementation of the Yamamoto estimator is performed using multiple FFTs (Fast Fourier Transform), each measuring the LOS-weighted clustering along different axes as presented in Bianchi et al. (2015). Thus, the computation of the monopole and quadrupole can be written in terms of $N \log N$ processes (where N is the number of grid-cells used to discretise the galaxy field), which is significantly faster than performing the sum over galaxies used in previous analyses (Beutler et al. 2014).

We use a random catalogue of number density of $\bar{n}_s(\mathbf{r}) = \alpha^{-1} \bar{n}(\mathbf{r})$ with $\alpha^{-1} \simeq 50$. We place the LOWZ and CMASS galaxy samples on 1024^3 grids, of box side $L_b = 2300 h^{-1}$ Mpc for the LOWZ galaxies, and $L_b = 3500 h^{-1}$ Mpc to fit the CMASS galaxies. This corresponds to a grid-cell resolution of $3.42 h^{-1}$ Mpc for the CMASS galaxies and $2.25 h^{-1}$ Mpc for the LOWZ galaxies. The fundamental wave-lengths are therefore $k_f = 1.795 \cdot 10^{-3} h\text{Mpc}^{-1}$ and $k_f = 2.732 \cdot 10^{-3} h\text{Mpc}^{-1}$ for the CMASS and LOWZ galaxies, respectively. We have checked that for $k \leq 0.3 h\text{Mpc}^{-1}$, doubling the number of grid-cells per side, from 1024 to 2048, produces a negligible change in the power spectrum, $\ll 1\%$. This result indicates that using 1024^3 grid-cells provides sufficient resolution at the scales of interest. We apply the Cloud-in-Cells scheme (CiC) to associate galaxies to grid-cells, and bin the power spectrum k -modes in 60 bins between the fundamental frequency k_f and a maximum frequency of $k_M = 0.33 h\text{Mpc}$, with width $\Delta \log_{10} k = [\log_{10}(k_M) - \log_{10}(k_f)] / 60$.

We limit the scales fitted as follows: our procedure for determining the largest scale we use for the fitting process is based on limiting the impact of the systematic weights, and is presented in Appendix A. We limit scales to $k > 0.02 h\text{Mpc}^{-1}$ for the monopole and $k > 0.04 h\text{Mpc}^{-1}$ for the quadrupole. The smaller (larger) the minimum scale (k -value) included, the more k -modes are used and therefore the smaller the statistical errors of the estimated parameters. However, small scales are poorly modeled in comparison to large scales, such that we expect the systematic errors to grow as the minimum scale decreases. Therefore, we empirically find a compromise between these two effects such that the systematic offset induced by poorly modelled non-linear behaviour is smaller than the statistical error. To do so, we perform different best-fit analysis for different minimum scales and check that the best-fit parameters of interest does not change significantly (compared to the statistical errors) as a function of this minimum scale.

4 THE POWER SPECTRUM MULTIPOLES

The top sub-panel of Fig. 1 presents the power spectrum monopole (blue squares) and quadrupole (red circles) for LOWZ and CMASS DR12 data measurements (top and bottom panels as labeled) from the combination of the NGC and SGC data. This combination has performed by aver-

aging the NGC and SGC power spectra weighting by their effective area,

$$P^{(\ell)} = (P_{\text{NGC}}^{(\ell)} A_{\text{NGC}} + P_{\text{SGC}}^{(\ell)} A_{\text{SGC}}) / (A_{\text{NGC}} + A_{\text{SGC}}), \quad (7)$$

where A_{NGC} and A_{SGC} are the effective areas of the NGC and SGC, respectively, whose values are $A_{\text{NGC}}^{\text{lowz}} = 5836 \text{ deg}^2$, $A_{\text{SGC}}^{\text{lowz}} = 2501 \text{ deg}^2$, $A_{\text{NGC}}^{\text{cmass}} = 6851 \text{ deg}^2$ and $A_{\text{SGC}}^{\text{cmass}} = 2525 \text{ deg}^2$. The best-fit model predictions are shown by the solid lines, taking the average of the models fitted using the covariance extracted from QPM and MD-PATCHY mocks with parameters as reported in Table 1 in §7. Details about the models are presented in §5, and covariance matrices in §6.1. The blue solid line shows the model for the monopole and the red solid line for the quadrupole. Error-bars correspond to the *rms* of the mocks, averaging between those calculated using covariance matrices determined with QPM or MD-PATCHY mocks. The comparison of the *rms* of the QPM and MD-PATCHY mocks can be found in Fig. 4 and is discussed in §6.1.

In the lower sub-panels, we present the fractional differences between the data and the best-fit model. For both LOWZ and CMASS samples, the model is able to reproduce the monopole data points up to $k \simeq 0.24 \text{ hMpc}^{-1}$, within 3% accuracy (indicated by the black dotted horizontal lines). The model reproduces the measured quadrupole with an accuracy of $\sim 10\%$ for the LOWZ sample and of $\sim 5\%$ for the CMASS sample. However, the signal-to-noise ratio of the observed quadrupole is not sufficiently high to determine if the observed fluctuations are statistical or systematics of the model. For LOWZ and CMASS samples, the fitting process ignores the large scales ($k \leq 0.02 \text{ hMpc}^{-1}$ for the monopole and $k \leq 0.04 \text{ hMpc}^{-1}$ for the quadrupole) because of the effects of star contamination as it has been discussed in §2.1 (see Appendix A for a further discussion on how these limits have been decided). The effects of the fiber collisions on the best-fit parameters of the models are discussed in Appendix B.

5 MODELLING THE POWER SPECTRUM MULTIPOLES

In this section we present the model used to analyse the monopole and quadrupole power spectra in §4. The modelisation is done in the following four steps.

(i) In §5.1 we present the galaxy bias model that maps the dark matter theoretical predictions into galaxy statistical observables.

(ii) In §5.2 we present the model that relates the real space statistical moments with redshift-space ones.

(iii) In §5.3 we incorporate AP parameters in order to allow changes due to inaccuracies when converting redshifts into distances by assuming a different value of Ω_m than the actual one.

² The areas for both samples were initially planned to be the equal, as both samples are coming from the same spectroscopic pointing. However, due to difficulties during the early phases of the project, the sky area of the LOWZ sample lags that of the full survey by approximately 1000 deg^2 (Anderson et al. 2014).

(iv) In §5.4 we describe how the window survey mask is applied in order to account for observational effects due to the geometry of the survey.

5.1 The bias model

We assume an Eulerian non-linear and non-local bias model proposed by McDonald & Roy (2009) and previously used for analysing the power spectrum multipoles and bispectrum of DR11 CMASS BOSS galaxies (Beutler et al. 2014; Gil-Marín et al. 2015a). A priori the non-local galaxy bias model depends on 4 free parameters: the linear bias b_1 , the non-linear bias b_2 and non-local bias parameters b_{s2} and b_{3nl} . In order to reduce the number of free bias parameters, we assume that the bias is local in Lagrangian space, which sets the values of b_{s2} and b_{3nl} given the linear bias coefficient, b_1 . This assumption has been validated using N-body simulations, and it provides consistent results between the power spectrum and bispectrum for the CMASS sample (Gil-Marín et al. 2014, 2015a). In case the condition of local Lagrangian bias were relaxed, the parameters b_{s2} and b_{3nl} would be treated as free parameters, increasing, consequently, the number of free parameters of the bias model. In such case, the model would account for a more general galaxy biasing, but the error-bars on the parameters of interest would also increase. Since, the results of the power spectrum and bispectrum of mocks and N-body simulations suggest that the bias model of galaxies and haloes is consistent with local Lagrangian, we also assume it for the data.

5.2 Modelling the redshift space distortions

The mapping from real space to redshift space quantities involves the power spectrum of the velocity divergence. We assume that there is no velocity bias between the underlying dark matter field and the galaxy field at least on the relatively large scales of interest. We follow the same redshift space modelling that in previous analysis (Beutler et al. 2014; Gil-Marín et al. 2015a), described in Taruya, Nishimichi & Saito (2010) and Nishimichi & Taruya (2011), which provides a prediction for the redshift space power spectrum in terms of the matter-matter, velocity-velocity and matter-velocity non-linear power spectra. Expressions for the non-linear power spectra used in this paper, were presented in Gil-Marín et al. (2015a); the model for the non-linear matter quantities was obtained using resummed perturbation theory at 2-loop level as described in Gil-Marín et al. (2012). The necessary linear power spectrum input was computed using CAMB (Lewis, Challinor & Lasenby 2000).

We account for the Fingers-of-God (hereafter FoG), through the Lorentzian damping factor, as described in Gil-Marín et al. (2015a). This factor has one free parameter referred as σ_{FoG} . With this parameter we aim to describe the non-linear damping due to the velocity dispersion of satellite galaxies inside host haloes. However we treat this factor as an effective parameter that encode our poor understanding of the non-linear RSD and we marginalised over.

In this paper we consider that the shot noise contribution in the power spectrum monopole may be modified from that of a pure Poisson sampling. We parametrise this deviation through a free parameter, A_{noise} , i.e., $P_{\text{noise}}^{(0)} =$

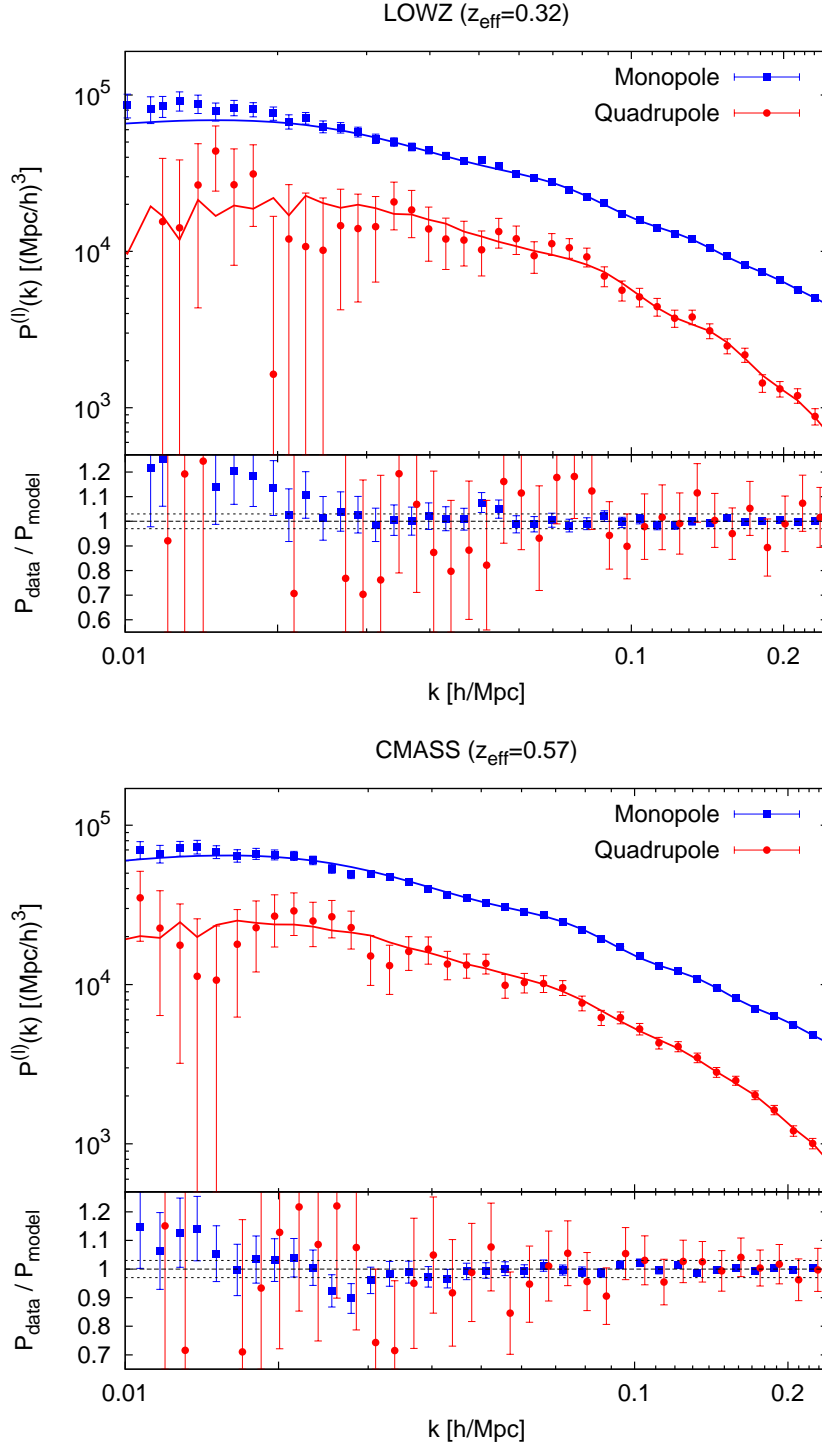


Figure 1. The top sub-panels display the measured LOWZ- (top panel) and CMASS-DR12 (bottom panel), monopole (blue squares) and quadrupole (red circles) power spectra. For both cases, the measurements correspond to a combination of the northern and southern galaxy caps according to their effective areas as presented in Eq.7. The error-bars are the average values of the dispersion among realizations of the QPM and MD-PATCHY mocks. The red and blue solid lines correspond to the best-fit model using the parameters listed in Table 1, for $k_{\text{max}} = 0.24 h\text{Mpc}^{-1}$. For simplicity, we plot the average between models corresponding to the parameters obtained using QPM and MD-PATCHY covariance matrices. The bottom sub-panels show the ratio between the power spectrum multipoles measurements and the best-fit model presented in the top sub-panel. The quadrupole symbols have been displaced horizontally for clarity. The dotted black lines represent a 3% deviation.

$(1 - A_{\text{noise}})P_{\text{Poisson}}^{(0)}$, where the terms $P_{\text{Poisson}}^{(0)}$ is the Poisson predictions for the shot noise as is presented in Eq. 6. For $A_{\text{noise}} = 0$ we recover the Poisson prediction, whereas when $A_{\text{noise}} > 0$ we obtain a sub-Poisson shot noise term and $A_{\text{noise}} < 0$ a super-Poisson noise term.

5.3 The Alcock-Paczynski effect

The AP effect (Alcock & Paczynski 1979) is caused by converting redshift into distance using a different cosmology from the actual one, which introduces a spurious anisotropy in the power spectrum that can be measured. Along the LOS, the observed signal is sensitive to the Hubble parameter through $\propto H^{-1}(z)$, when the clustering is measured on scales that are small compared with cosmological changes in the distance-redshift relationship. On the other hand, in the angular direction the distortions depend on the angular distance parameter, $D_A(z)$. When a fiducial model is assumed to convert redshifts into distances, the AP effect can be described by the dilation scales,

$$\alpha_{\parallel} \equiv \frac{H^{\text{fid}}(z)r_s^{\text{fid}}(z_d)}{H(z)r_s(z_d)}, \quad (8)$$

$$\alpha_{\perp} \equiv \frac{D_A(z)r_s^{\text{fid}}(z_d)}{D_A^{\text{fid}}(z)r_s(z_d)}, \quad (9)$$

where α_{\parallel} and α_{\perp} are the parallel- and perpendicular-to-the-LOS dilation scales, respectively. Here, $H^{\text{fid}}(z)$ and $D_A^{\text{fid}}(z)$ are the fiducial values (those corresponding to the assumed cosmology to convert redshifts into distances) of the Hubble constant and the angular diameter distance at a given redshift z , respectively. On the other hand, the fiducial sound horizon at the baryon-drag redshift is given by $r_s^{\text{fid}}(z_d)$. The factors α_{\parallel} and α_{\perp} describe how the true wave-length modes, k'_{\parallel} and k'_{\perp} , have been distorted into the observed ones, k_{\parallel} and k_{\perp} : $k_{\parallel} = \alpha_{\parallel}k'_{\parallel}$ and $k_{\perp} = \alpha_{\perp}k'_{\perp}$, by the effect of assuming a different cosmological model.

This component of observed anisotropy is modelled through the α_{\parallel} and α_{\perp} parameters (see eq. 60 of Beutler et al. 2014). The geometric AP effect also affects the BAO scale, and the assumed distance-redshift relation has the potential to shift the BAO peak position differently in the monopole and quadrupole moments of the observed comoving clustering signal. Therefore, the AP parameters are simultaneously measured in our analysis, even though our focus is on measuring the RSD. Analyses that do not wish to measure the RSD signal and focus on the BAO scale can make use of reconstruction and therefore, in general, provide better measurements of the AP effect (e.g. Cuesta et al. 2015; Gil-Marín et al. 2015b). We will comment on the potential differences further in §7.3.

Assuming the fiducial cosmology described in §2.3, the fiducial values for $H(z)$ and $D_A(z)$ are, $H^{\text{fid}}(z_{\text{lowz}}) = 79.49 \text{ km s}^{-1} \text{ Mpc}^{-1}$, $D_A^{\text{fid}}(z_{\text{lowz}}) = 999.23 \text{ Mpc}$ for the LOWZ sample at $z_{\text{lowz}} = 0.32$, and $H^{\text{fid}}(z_{\text{cmass}}) = 92.25 \text{ km s}^{-1} \text{ Mpc}^{-1}$, $D_A^{\text{fid}}(z_{\text{cmass}}) = 1398.43 \text{ Mpc}$ for the CMASS sample at $z_{\text{cmass}} = 0.57$. The value for the fiducial sound horizon distance is $r_s^{\text{fid}}(z_d) = 148.11 \text{ Mpc}$.

5.4 The survey geometry

The estimator presented in §3 only provides an unbiased prediction of the true underlying power spectrum without any survey geometry effects. At intermediate and large scales, the measurement is affected by the shape of the survey, especially for high order multipoles. Given a theoretical anisotropic power spectrum $P^{\text{theo.}}(\mathbf{k}')$, the observed power spectrum due to the effects of the survey is windowed through the following expression,

$$P^{\text{win.}}(\mathbf{k}) = \int \frac{d^3\mathbf{k}'}{(2\pi)^3} P^{\text{theo.}}(\mathbf{k}') |W(\mathbf{k} - \mathbf{k}')|^2, \quad (10)$$

where W is defined as,

$$W(\mathbf{k}) \equiv \frac{\alpha}{I_2^{1/2}} \int d^3\mathbf{r} \bar{n}_s(\mathbf{r}) e^{i\mathbf{k}\cdot\mathbf{r}}. \quad (11)$$

We refer to $|W|^2$ as the window function, which satisfy the normalization condition, $\int d^3\mathbf{k}' / (2\pi)^3 |W(\mathbf{k}')|^2 = 1$, imposed by the definition of the factor I_2 in Eq. 4. The functional provided by $P^{\text{win.}}[P^{\text{theo.}}]$ in Eq. 10 is a convolution. Therefore, the convolution theorem can be apply making use of FFT techniques, which allows the computation in a minutes-time scale per model $P^{\text{theo.}}$.

We assume that the monopole and quadrupole provide all the information about the full μ -shape of the power spectrum. Thus we can write,

$$P^{\text{theo.}}(\mathbf{k}) = P^{(0)\text{theo.}}(k) + P^{(2)\text{theo.}}(k) \mathcal{L}_2(\mu). \quad (12)$$

We can define a windowed power spectrum ℓ -multipole as,

$$P^{(\ell)\text{win.}}(k) = \frac{2\ell + 1}{2} \int d\mu_k \mathcal{L}_{\ell}(\mu_k) P^{\text{win.}}(\mathbf{k}), \quad (13)$$

where $\mu_k \equiv \hat{r}_z \cdot \hat{\mathbf{k}}$. From Eq. 13 it is clear to see that both $P^{(0)\text{win.}}$ and $P^{(2)\text{win.}}$ have contributions from both $P^{(0)\text{theo.}}$ and $P^{(2)\text{theo.}}$. Eq. 13 provides a full description of the effect of the window in the monopole and quadrupole. However, for practical reasons, is convenient to use this equation to calibrate a matrix that is able to relate the $P^{(\ell)\text{win.}}$ at a given k -bin from an arbitrary shape of $P^{(\ell)\text{theo.}}$. Using Eq. 13 we write the matrix elements,

$$\begin{aligned} \mathcal{W}_{ij}^{\ell\ell'} &\equiv \left[\frac{2\ell' + 1}{2} \int d\mu_k \mathcal{L}_{\ell'}(\mu_k) \int d^3\mathbf{k}' |W(\mathbf{k} - \mathbf{k}')|^2 \right. \\ &\quad \times \left. P^{(\ell)\text{theo.}}(k') \mathcal{L}_{\ell}(\mu') \Theta_{\text{TH}}(k_i - k') \right] / P^{(\ell')\text{theo.}}(k_j), \end{aligned} \quad (14)$$

where $\Theta_{\text{TH}}(k_i - k')$ is a top hat function around the k_i -bin: $\Theta_{\text{TH}}(k_i - k')$ is 1 when k' belongs to k_i -bin and 0 otherwise. In order to form a window-matrix which is able to mimic the behaviour described by Eq. 13 we have used 1000 k -bins between k_f and $k = 0.5 h \text{ Mpc}^{-1}$ as an input of k_j and 60 output k_i -bins which coincides with the k -values where we measure the dataset. Using the calibrated values of the window matrix described by Eq. 14 we write the windowed monopole and quadrupole power spectra as,

$$\begin{aligned} P^{(0)\text{win.}}(k_i) &= \sum_j \mathcal{W}_{ij}^{00} P^{(0)\text{theo.}}(k_j) + \sum_j \mathcal{W}_{ij}^{02} P^{(2)\text{theo.}}(k_j), \\ P^{(2)\text{win.}}(k_i) &= \sum_j \mathcal{W}_{ij}^{20} P^{(0)\text{theo.}}(k_j) + \sum_j \mathcal{W}_{ij}^{22} P^{(2)\text{theo.}}(k_j). \end{aligned} \quad (15)$$

Note that Eq. 13 and 15 describe the same survey window effect, but the latter one is much faster to be applied to minimization and MCMC algorithms. In this paper we always use combined window that we obtain by weighting the individual windows of NGC and SCG by their area. Since this is what we do with the power spectrum measurements, the combined window reproduce by definition the combined power spectrum.

The matrix terms in Eq. 14 depend, in principle, on the choice of theoretical power spectrum, $P^{(\ell)\text{theo}}$. However this dependence is expected to be weak, as the term $P^{(\ell)\text{theo}}$ appears in both denominator and numerator, and the part of the signal in $W_{ij}^{\ell\ell'}$ coming from $P^{(\ell)\text{theo}}$ is cancelled. In order to quantify this, we have built two window matrices with different power spectra, whose values are within 2σ of the data and no significant differences were observed.

Fig. 2 shows the effect of the LOWZ (left panel) and CMASS (right panel) DR12 samples on the power spectrum monopole and quadrupole. The upper panel shows a toy model input power spectrum monopole (blue solid lines) and quadrupole (red solid lines) and its output according to Eq. 15 (blue and red dashed lines). The lower panels show the ratio between the input and the output power spectrum multipole. We see that for CMASS the effect, both in the monopole and in the quadrupole, is smaller than for the LOWZ. This is due to the size of the sample. The larger the sample is, the smaller is the effect of the mask. At $k \simeq 0.2 h\text{Mpc}^{-1}$, the effect of the window is near 0% for the monopole in CMASS, $\sim 5\%$ for the quadrupole in CMASS, $\sim 7\%$ for the monopole in LOWZ and $\sim 10\%$ for the quadrupole in LOWZ. At large scales, the windowed power spectrum predicted for the quadrupole has oscillatory behaviour, a consequence of the lack of μ -modes in the k -bins at these scales: since the k -binning is logarithmic, the number of fundamental k -modes contained at large scales is much smaller than that at small scales. As a consequence, at these large scales the constraint $\int d\mu \mathcal{L}_\ell(\mu) \mathcal{L}_{\ell'}(\mu) = \delta_{\ell\ell'}$ is not satisfied for $\ell, \ell' > 0$ with sufficient precision. The behaviour can be corrected by renormalising, both data and window by the sum of squared Legendre polynomials over the μ -modes: μ -modes $\sum_{\mu\text{-modes}} \mathcal{L}_\ell^2(\mu)$. However, since for this paper we only use quadrupole data for $k > 0.04 h\text{Mpc}^{-1}$, where the μ -modes contained in the k -bins are large enough, the correction is not significant enough to be worth including. In any case, since the correction would have to be applied to both data and window, the relative ratio between theory and data would be unaffected by this correction.

In this paper we do not correct the power spectrum multipoles for the integral constrain, which only produce a significant effect at scales comparable to the size of the survey (see e.g. Peacock & Nicholson 1991), which in our case is $k_f \sim 0.002 h\text{Mpc}^{-1}$. Since the largest scales we consider are 10 and 20 times smaller for the monopole and quadrupole, respectively, in our analysis the integral constrain is a subdominant component compared to other effects such as systematic weights.

6 PARAMETER ESTIMATION

In this section we describe how the parameters of interest and their errors, including the AP parameters and $f\sigma_8$ are estimated. We also present a systematic test on the power spectrum model presented in §5 using the galaxy mocks.

6.1 Covariance Matrices

The covariance matrix of the monopole and quadrupole is computed using the different realizations of the two sets of galaxy mocks described in §2.2. We take into account the covariance of the monopole and quadrupole k -bins and also the cross-covariance between these two. Each element of the covariance matrix is calculated from the mocks,

$$C_{i,j}^{\ell\ell'} = \frac{1}{N_m - 1} \sum_{m=1}^{N_m} [P_m^{(\ell)}(k_i) - \langle P^{(\ell)}(k_i) \rangle] \times [P_m^{(\ell')} (k_j) - \langle P^{(\ell')} (k_j) \rangle], \quad (16)$$

where $\langle P^{(\ell)}(k) \rangle \equiv \sum_m^{N_m} P_m^{(\ell)}(k)/N_m$ is the mean of the ℓ -multipoles among realizations, and N_m is the number of independent realizations. The full covariance matrix for the monopole and quadrupole can be written in terms of the matrices $C^{\ell\ell'}$, for $\ell = 0, 2$, as,

$$C = \begin{pmatrix} C^{00} & C^{02} \\ C^{20} & C^{22} \end{pmatrix}. \quad (17)$$

For the QPM mocks the number of independent realization is $N_m = 1000$, whereas for MD-PATCHY is $N_m = 2048$. In both cases the number of elements is much larger than the total number of bins, n_b , which for this work is $n_b = 120$.

Since the covariance matrix C is estimated from a set of mocks, its inverse C^{-1} is biased due to the limited number of realizations. We account for this effect by applying the correction proposed by Hartlap, Simon & Schneider (2007). In addition to this scaling, we have to propagate the error in the covariance matrix to the error on the estimated parameters. We do this by scaling the variance for each parameter by the factor of eq. 18 of Percival et al. (2014). However, we observe that the correction due to this effect is subdominant, namely $\leq 2\%$.

The middle and top panels of Fig. 3 display the correlation coefficient matrices, $r_{i,j} \equiv C_{i,j}/[C_{i,i}C_{j,j}]^{1/2}$ for LOWZ and CMASS samples using the QPM mocks and the MD-PATCHY mocks as labeled. In all cases NGC and SCG have been combined into a single sample, as described in §4. We observe that the off-diagonal terms of the auto-covariance (the covariance between monopole-monopole and quadrupole-quadrupole) are significantly correlated at large scales because of the effect of the survey geometry, for both monopole and quadrupole. The off-diagonal terms of the cross-covariance between monopole and quadrupole present significantly smaller correlation.

As we go to smaller scales the auto- and cross-covariance off-diagonal terms are reduced for both LOWZ and CMASS samples because the effect of the survey window is less important. For $k \geq 0.2$ the auto-covariance off-diagonal elements start growing again because of the effect of mode coupling, which becomes more important as we go to smaller scales. At the same scales, the off-diagonal terms of cross-covariance stay very close to 0. This suggests that the mode

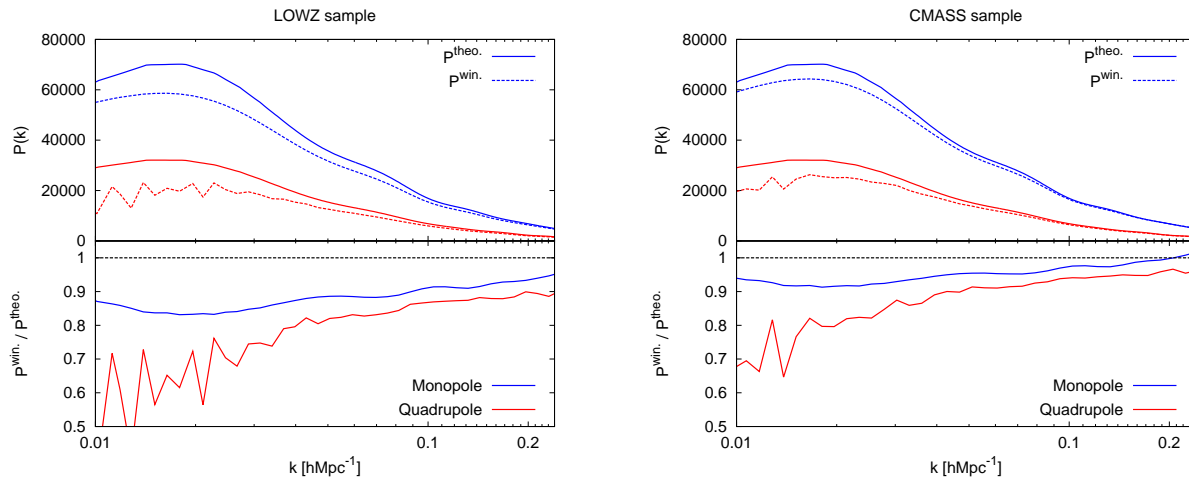


Figure 2. Top sub-panels: Effect of the window function on the monopole (blue lines) and on the quadrupole (red lines) for the LOWZ-DR12 sample (left panel) and for the CMASS-DR12 sample (right panel). The solid lines correspond to a toy-model for $P^{\text{theo.}(0)}$ and $P^{\text{theo.}(2)}$ in Eq. 12. The dashed lines correspond to $P^{(0)\text{win.}}$ and $P^{(2)\text{win.}}$ in Eq. 15. Lower sub-panels: Relative deviation between $P^{(\ell)\text{win.}}$ and its convolution with the window mask.

coupling induces a strong correlation between close k -modes in the monopole and quadrupole, but not a correlation between these two statistics until $k = 0.3 h\text{Mpc}^{-1}$.

The bottom panels of Fig. 3 show the ratio between the QPM and MD-PATCHY covariances for LOWZ and CMASS samples, as labeled, in order to stress their differences. We observe that most of the off-diagonal signal is very noisy, although some differences can be seen for those off-diagonal terms close to the diagonal. For both LOWZ and CMASS samples, both QPM and MD-PATCHY mocks predict the same degree of correlation on large scales. As we go to smaller scales some differences arise. At scales where $k \geq 0.1, h\text{Mpc}^{-1}$, the off-diagonal terms of the monopole auto-correlation matrix, tend to be more correlated in the QPM mocks than in the MD-PATCHY mocks, while the auto-correlation matrix estimates for the quadrupole are similar.

In Fig. 4 we show the percentile diagonal error for power spectrum multipoles, corresponding to the k -bins used in §4, relative the power spectrum multipole amplitude of the data. At large scales both QPM and MD-PATCHY prediction agree well for both the LOWZ and CMASS samples for both monopole and quadrupole. At small scales QPM mocks predict *higher* mode coupling in the monopole than MD-PATCHY and therefore the errors of the power spectrum monopole saturate *before* that of the MD-PATCHY predictions. The precision of the monopole exceeds 1% for $k \leq 0.13 h\text{Mpc}^{-1}$.

For the quadrupole the relative error predicted by QPM and MD-PATCHY mocks is very similar in all the range of scales studied.

Overall, the covariances extracted from QPM and MD-PATCHY mocks are similar and the main discrepancies are for the monopole at small scales. We are not able to discriminate which of these to sets of mocks is best.

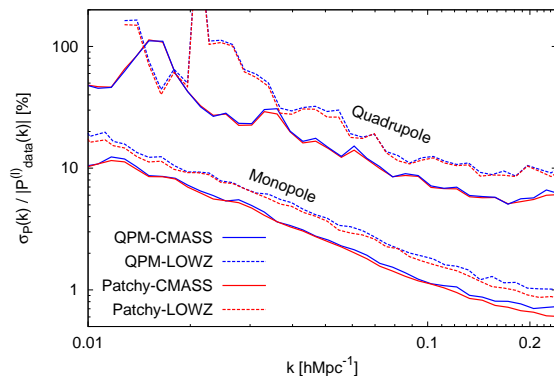


Figure 4. Percentile diagonal errors corresponding to the k -bins used in §4 in which the monopole and quadrupole have been measured for the mocks. Solid lines display the CMASS-DR12 statistics and dashed lines the LOWZ-DR12 ones. Red lines are the predictions inferred from the MD-PATCHY mocks, whereas the blue lines are according to QPM mocks.

6.2 Best-fit and error estimation

We model the amplitude and the shape of the power spectrum monopole and quadrupole through a set of 8 free parameters $\Psi = \{b_1, b_2, f, \sigma_8, A_{\text{noise}}, \sigma_{\text{FoG}}, \alpha_{\parallel}, \alpha_{\perp}\}$, which we briefly describe below.

(i) The galaxy bias is modelled using two bias parameters, b_1 and b_2 as described in §5.1. The value for the non-local bias parameters is set by the value of b_1 under the assumption of local Lagrangian bias.

(ii) The logarithmic growth factor f . This parameter can be predicted for a specific cosmological model (when the Ω_m value is known) if we assume a theory of gravity. In this paper we consider this as free parameter in order to test

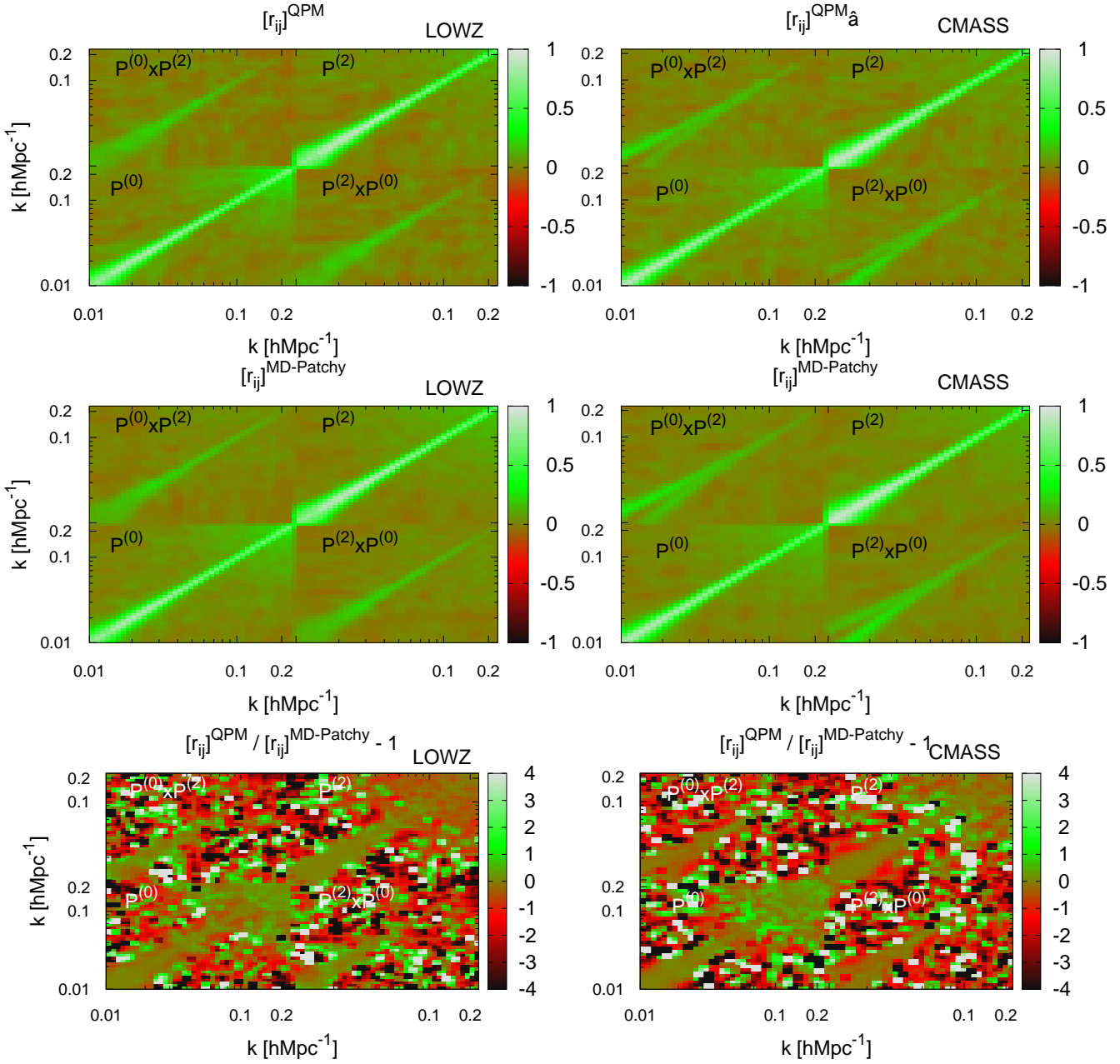


Figure 3. Correlation coefficients of the monopole-quadrupole covariance matrix from LOWZ-DR12 sample (left panels) and from the CMASS-DR12 sample (right panels), extracted from 1000 realizations of the QPM mocks and from 2048 realizations of the MD-PATCHY mocks. The top panels show the results for QPM mocks, the middle panels for the MD-PATCHY mocks, and the bottom panels their ratio.

potential deviations from GR, or, if assuming GR, for not using a prior on the Ω_m value.

(iii) The AP parameters, α_{\parallel} and α_{\perp} . As described in §5.3, through varying α_{\parallel} and α_{\perp} we are able to parametrise the anisotropy generated in the power spectrum multipoles by assuming an incorrect value of Ω_m .

(iv) The amplitude of primordial dark matter power spectrum, σ_8 .

(v) The amplitude of shot noise, A_{noise} , as described in §5.2

(vi) The Fingers-of-God parameter, σ_{FoG} , introduced in §5.2.

Note that although we allow f and σ_8 to vary independently, these two parameters are highly degenerate when constrained only using the power spectrum multipoles³. We will only quote the measured combined quantity $f\sigma_8$. Similarly, we will only report $b_1\sigma_8$, and $b_2\sigma_8$.

The other cosmological parameters, such as Ω_m , the spectral index n_s and the Hubble parameter h are fixed at the fiducial values described in §2.3 during the fitting process. In §7.1 we will vary the value of Ω_m to analyse the effect of such a change can produce in $f\sigma_8$. In this paper we always perform the parameter fitting process to the combined NGC+SGC sample, both for the mocks and for the data.

In order to preform the parameter estimation, we assume the monopole and quadrupole are drawn from a multivariate Gaussian distribution and use,

$$\chi^2(\Psi) = [\Delta P(\Psi)]\tilde{C}^{-1}[\Delta P(\Psi)]^t \quad (18)$$

where, $\Delta P(\Psi)$ is the vector whose elements contain the difference between the data and the model for the power spectrum monopole and quadrupole, and \tilde{C}^{-1} is the inverse covariance matrix. By minimizing the χ^2 function respect to Ψ we obtain the best-fit set of parameters. The errors associated to each parameter are computed by exploring the likelihood surface when a specific parameter is fixed and the other parameters can vary freely. The likelihood surface is explored using a SIMPLEX minimization algorithm. In order to ensure that the minima found are global and not local, we run the algorithm multiple time with different starting points and different starting variation ranges, and check for convergence.

6.3 Tests for the galaxy mocks

In this section we test for potential systematics of the model presented in §5 using the MD-PATCHY galaxy mocks. We start by comparing the power spectrum multipoles for the mean of the 1000 and 2048 realizations of the QPM and MD-PATCHY mocks, respectively, with the measurements of the DR12 data. This is shown in Fig. 5, where the power spectrum monopole and quadrupole are divided by a smooth linear power spectrum. The left and right panels show the measurements corresponding to LOWZ and CMASS samples, respectively. Blue symbols represent the measurements for the data corresponding to the monopole, whereas the red symbols represent the quadrupole. The black dashed and dotted lines show the mean values of the mocks for QPM and MD-PATCHY, respectively.

For the LOWZ sample the MD-PATCHY mocks describe accurately the data measurements for both monopole and quadrupole. The QPM mocks show some discrepancies with the data: QPM mocks systematically overestimate the monopole data by $\sim 10\%$ at $k \geq 0.02, h\text{Mpc}^{-1}$ and fail to describe the quadrupole for $k \geq 0.1 h\text{Mpc}^{-1}$. For the CMASS

sample, MD-PATCHY mocks describe well the monopole and quadrupole data. QPM mocks tend to overestimate both statistics by few percent. The version of QPM mocks used in this paper was not designed to describe redshift space distortion features with few percent accuracy, as this version of the MD-PATCHY mocks was. Because of this, we will only use the MD-PATCHY mocks multipole measurement to test the modelling of RSD.

We combine the model described in §5 with the measured mock power spectrum monopole and quadrupole, averaged over the 2048 realization of the MD-PATCHY mocks, in order to recover the $f\sigma_8$ parameter. Since we know the input cosmological parameters for the mock simulations, we can compare the obtained value with the expected one, and thus test which is the precision of the model when recovering $f\sigma_8$. Note that the measurements of the monopole and quadrupole of the mocks have been performed using the fiducial cosmology, which is different to the cosmology of the mocks as described in §2.2.

Fig 6 displays in blue symbols linked by solid blue lines the obtained $f\sigma_8$, α_{\parallel} and α_{\perp} parameters as a function of the minimum scaled used to fit the model to the measurements of the MD-PATCHY mocks. The error-bars correspond to the data error-bars scaled by a volume factor of $\sqrt{2048}$ in order to account for the volume difference. In order to mimic the data analysis, the large scales cuts $k_{\min} = 0.02 h\text{Mpc}^{-1}$ and $0.04 h\text{Mpc}^{-1}$ for the monopole and quadrupole, respectively, have been applied. In addition to α_{\parallel} , α_{\perp} , f and σ_8 , we allow b_1 , b_2 , A_{noise} and σ_{FoG} to vary, as we do for the data. The expected values for $f\sigma_8$ are shown in black dashed lines. For reference, 1% and 3% deviations from the expected $f\sigma_8$ are also shown in dot-dashed and dotted black lines, respectively.

For the LOWZ sample we see that the recovered value of $f\sigma_8$ agrees to $\leq 2\%$ accuracy with the true one for $k_{\max} \geq 0.16 h\text{Mpc}^{-1}$. We observe that if the truncation scale is $k_{\max} = 0.15 h\text{Mpc}^{-1}$, the model produces a systematically low value of $f\sigma_8$. However, this does not occur when the truncation scale is higher than this value. In particular, if the truncation scale is $k_{\max} \geq 0.20 h\text{Mpc}^{-1}$ the accuracy of the obtained $f\sigma_8$ is $\lesssim 1\%$, which is around 10 times smaller than the expected statistical error for this sample. We observe that α_{\perp} is constrained with $\lesssim 1\%$ accuracy, at all studied scales. α_{\parallel} presents $\simeq 3\%$ deviation from its fiducial value at $k_{\max} = 0.24 h\text{Mpc}^{-1}$, and decreases to $\leq 1\%$ as the scale of truncation is increased.

For the CMASS sample we see that the recovered value of $f\sigma_8$ agree with $\lesssim 1\%$ accuracy for truncation scales within the whole range of scales studied. Given the statistical errors for the CMASS sample, this systematic error is around 8 times smaller. As for the LOWZ case, α_{\perp} is recovered within $\leq 1\%$ accuracy and α_{\parallel} within $\leq 2\%$, in all the range of studied scales.

Since the observed systematic errors for both LOWZ and CMASS samples are much smaller than the statistical errors obtained for the data, we do not correct $f\sigma_8$ by any systematic shift.

Fig. 7 shows the distribution of parameters $f(z)\sigma_8(z)$, $H(z)r_s(z_d)$ and $D_A(z)/r_s(z_d)$ for the 2048 realizations of the MD-PATCHY mocks in the LOWZ and CMASS samples. The blue crosses represent the best-fit parameter set for each realization of the mocks, whereas the red cross is

³ f and σ_8 are fully degenerated only in the large-scale limit, when Kaiser formula is still valid. At smaller scales the non-linear corrections break this degeneration. However, the signal-to-noise of the power spectrum at these scales is not sufficiently high to make reasonable constrains on f and σ_8 alone, since the degeneration is poorly broken. Because of this we refer to these two parameters as highly degenerate but not fully degenerate.

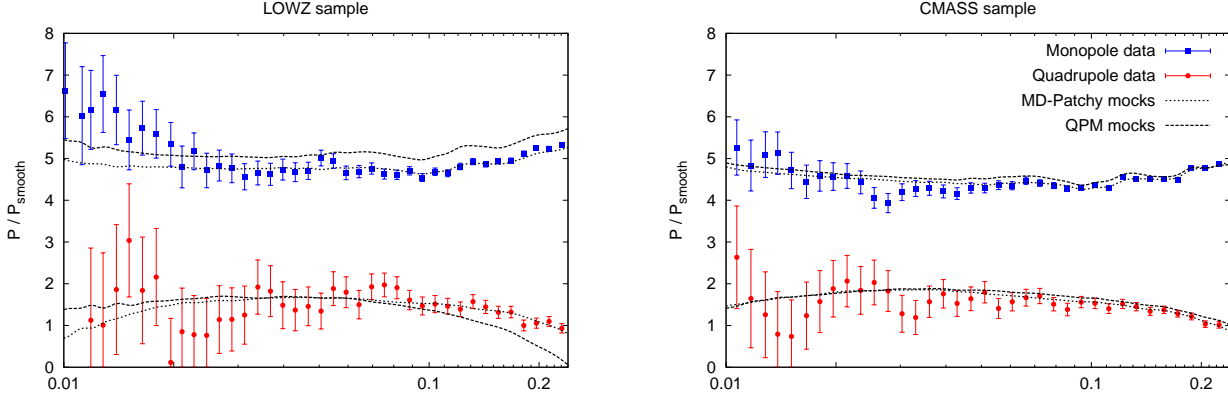


Figure 5. Performance of the QPM (black dashed lines) and MD-PATCHY (black dotted lines) mocks compared to the data, blue squares for the monopole and red circles for the quadrupole. The left and right panels display the results for the LOWZ and CMASS samples, respectively. For clarity, the amplitude of the power spectrum multipoles have been normalised by a smoothed linear power spectrum, P_{smooth} .

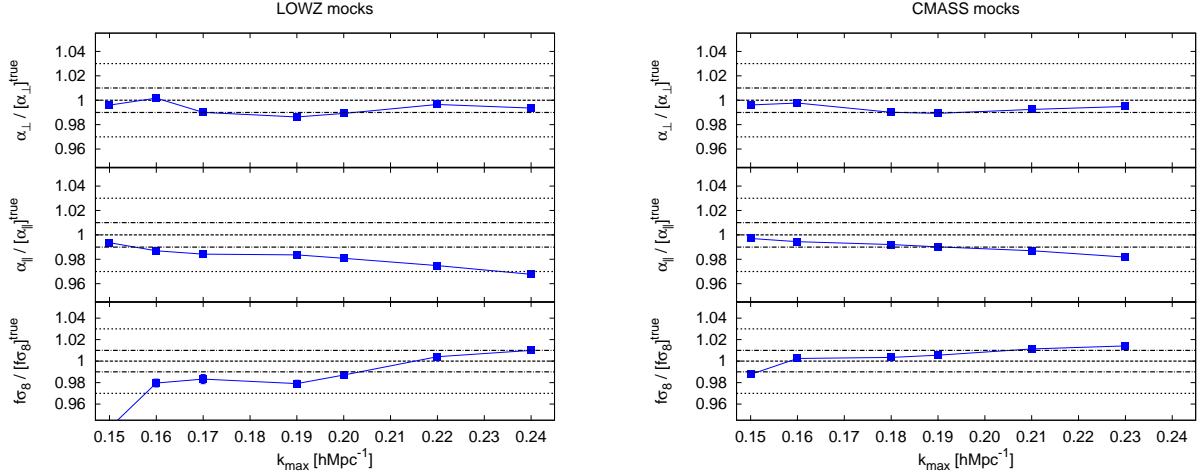


Figure 6. Best-fit α_{\perp} , α_{\parallel} and $f\sigma_8$ parameters as a function of the minimum scale (maximum k) used for describing the LOWZ- (left panels) and CMASS (right panels) monopole and quadrupole power spectra predicted by the average of 2048 realizations of the MD-PATCHY mocks (blue squares linked by solid lines). In order to mimic the analysis of the data, the largest scales used for the fit are $k_{\text{min}} = 0.02 \text{ hMpc}^{-1}$ for the monopole and $k_{\text{min}} = 0.04 \text{ hMpc}^{-1}$ for the quadrupole. All values normalised by the corresponding true expected value. Horizontal dashed, dot-dashed and dotted lines show the 0%, 1% and 3% deviations, respectively, with respect to the corresponding fiducial value.

for the data. The shapes of the clouds formed by the blue crosses provide information of how these parameters are degenerate. Thus, these plots show that the measurements of $f\sigma_8$, $H(z)r_s(z_d)$ and $D_A(z)/r_s(z_d)$ are strongly correlated. Assuming that the data results can be approximated by a multivariate Gaussian likelihood, in §7.5 we provide the covariance matrix among these 3 parameters for the measurements from the data.

Fig. 8 shows the two-dimensional parameter space of $b_1\sigma_8$ and $f\sigma_8$ for the 2048 realizations of the MD-PATCHY mocks in the LOWZ and CMASS samples.

We see that when the AP parameters are set to 1, the scatter between best-fit values from different mocks reduces significantly forming a small cloud (green crosses) which is

contained by the blue one. The red crosses represent the actual values for the data when the MD-PATCHY covariance is used. In both cases we see that the data points lies well within the clouds formed by the different realizations of the MD-PATCHY mocks.

7 BOSS DR12 MEASUREMENTS

The values of the parameters of the model corresponding to the fits to the data presented in Fig. 1 are listed in Table 1, where the minimum cut-off scale used for the fit is $k_{\text{max}} = 0.24 \text{ hMpc}^{-1}$. We observe that the difference between parameters (using QPM and MD-PATCHY covariances)

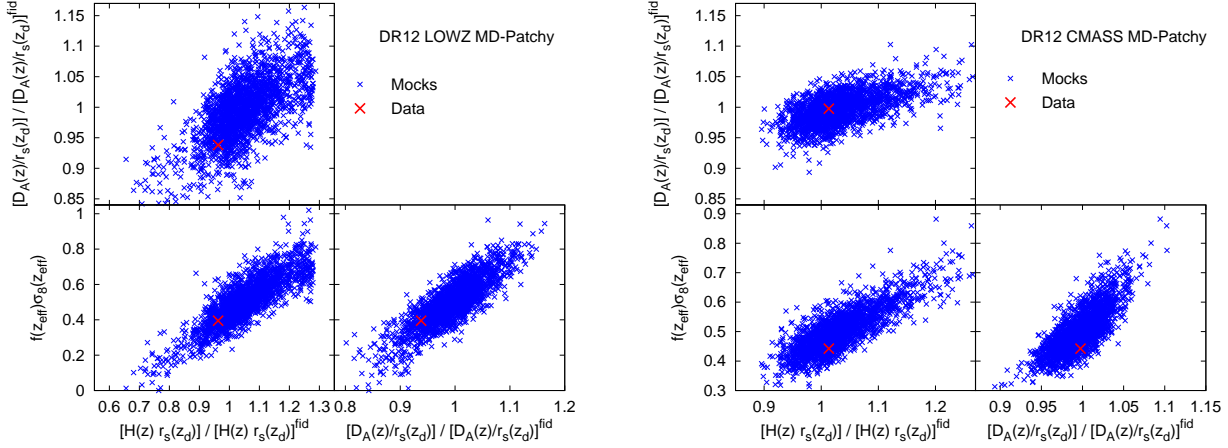


Figure 7. Two dimensional distribution of $f(z)\sigma_8(z)$, $H(z)r_s(z_d)$ and $D_A(z)/r_s(z_d)$, for the LOWZ and CMASS samples, left and right panels, respectively. The blue points represent the best-fit solutions of 2048 independent MD-PATCHY mocks realizations. The red crosses are the results for the data. The scatter of the mocks gives an idea of how these parameters are degenerate. Both mocks and data have been analysed using the MD-PATCHY covariance.

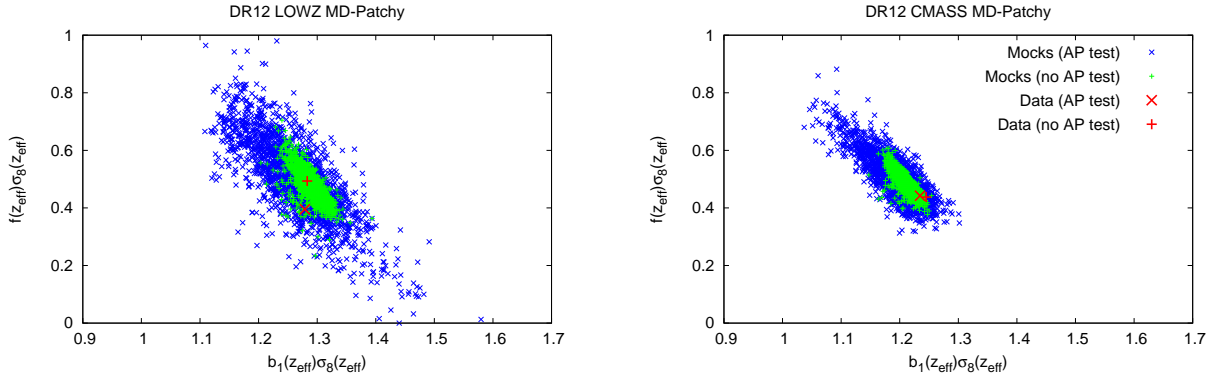


Figure 8. Two-dimensional distribution for the parameter space corresponding to $b_1\sigma_8$ and $f\sigma_8$. Left and right panels display the results for the LOWZ and CMASS samples. Blue \times -symbols correspond to the best-fit solution for each realization (out of 2048) of the MD-PATCHY mocks when all parameters are freely varied. The green $+$ -symbols correspond to the best-fit solution when the AP parameters, α_{\parallel} and α_{\perp} are set their fiducial values, respectively. The red \times -symbol display the best-fit solution for the data sample when all the parameters are varied. The red $+$ -symbol display the best-fit solution for the data sample when the AP parameters have been set to their fiducial values. In all the cases the covariance matrix have been inferred using the MD-PATCHY mocks.

and their error-bars is not significant. This indicates that the impact of the different covariance matrices in the parameter estimation is sub-dominant compared to other effects, such as the scale where the fitting process is truncated, or systematics of the model itself.

Table 2 displays the best-fit results at $k_{\max} = 0.24 h\text{Mpc}^{-1}$, with $H(z)r_s(z_d)$ and $D_A(z)/r_s(z_d)$ set to the fiducial cosmology prediction. As in Table 1, the differences between the parameters and their errors obtained using either QPM and MD-PATCHY mocks are not significant.

In Fig. 9 we show how the best-fit values of $f\sigma_8$ and the AP parameters, α_{\parallel} and α_{\perp} , change with the minimum scale considered.

From the left panels of Fig. 9 we observe that when

varying k_{\max} from $0.15 h\text{Mpc}^{-1}$ to $0.24 h\text{Mpc}^{-1}$, the best-fit value of $f\sigma_8$ is very stable compared to the size of the error-bars. This behaviour applies when the AP parameters are varied and also when they are fixed to their fiducial value. When the AP parameters are varied the best-fit value of $f\sigma_8$ is consistently low by $\sim 1\sigma$ respect to *Planck15*+GR prediction. We also observe that, whereas α_{\parallel} is consistent with unity for all values of k_{\max} studied, α_{\perp} presents a low value of $2\sigma - 3\sigma$ respect to the fiducial cosmology prediction. When the AP parameters, α_{\parallel} and α_{\perp} , are set 1, the LOWZ-sample $f\sigma_8$ parameter, is shifted $\sim 1\sigma$ upwards and is more in accordance with the *Planck15* cosmology prediction. We observe that this effect is independent of the model truncation scale. In §7.1 we will reanalyze the data assuming

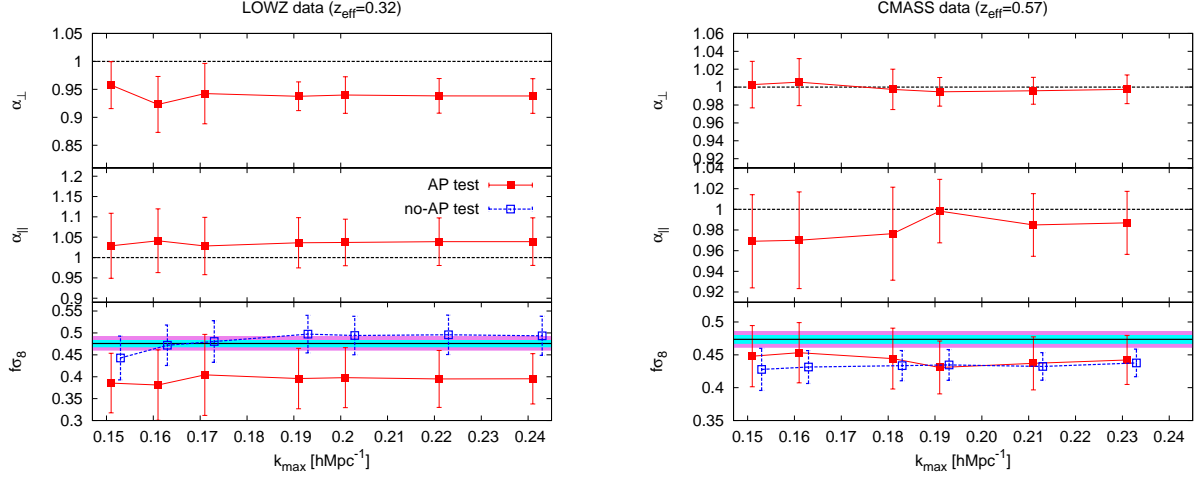


Figure 9. Power spectrum monopole and quadrupole best-fit parameters as a function of the minimum scale considered, k_{\max} . The results for the LOWZ- (left panels) and CMASS-DR12 (right panel) BOSS data are shown in red solid lines in combination with red filled symbols. In the $f\sigma_8$ panel we also show in dashed blue lines and empty blue symbols the best-fit values when the AP parameters have been set to their fiducial value. In this case, the symbols have been displaced horizontally for visualization reasons. For all the cases the largest scales used for the fitting are $k_{\min} = 0.02 \text{ hMpc}^{-1}$ for the monopole and $k_{\min} = 0.04 \text{ hMpc}^{-1}$ for the quadrupole. In the $f\sigma_8$ sub-panels we show as a black solid line the predictions from *Planck15*. The cyan and magenta bands represent the 1σ and 2σ error-bars, respectively, around the *Planck15* best-fit solution.

Sample (Cov.)	LOWZ (QPM)	LOWZ (MD-PATCHY)	CMASS (QPM)	CMASS (MD-PATCHY)
$f(z_{\text{eff}})\sigma_8(z_{\text{eff}})$	0.392 ± 0.061	0.395 ± 0.064	0.445 ± 0.038	0.442 ± 0.037
$H(z_{\text{eff}})r_s(z_d) [10^3 \text{ kms}^{-1}]$	11.48 ± 0.55	11.33 ± 0.56	13.99 ± 0.44	13.84 ± 0.43
$D_A(z)/r_s(z_d)$	6.38 ± 0.18	6.33 ± 0.19	9.43 ± 0.15	9.42 ± 0.15
$\alpha_{\parallel}(z_{\text{eff}})$	1.025 ± 0.052	1.039 ± 0.054	0.977 ± 0.030	0.987 ± 0.030
$\alpha_{\perp}(z_{\text{eff}})$	0.945 ± 0.027	0.938 ± 0.028	0.999 ± 0.016	0.998 ± 0.016
$b_1\sigma_8(z_{\text{eff}})$	1.283 ± 0.032	1.279 ± 0.037	1.218 ± 0.022	1.225 ± 0.020
$b_2\sigma_8(z_{\text{eff}})$	-0.19 ± 0.64	-0.38 ± 0.36	0.67 ± 0.74	0.40 ± 0.66
A_{noise}	-0.30 ± 0.22	-0.43 ± 0.21	-0.041 ± 0.078	-0.057 ± 0.093
$\sigma_{\text{FoG}}(z_{\text{eff}}) [\text{Mpch}^{-1}]$	3.94 ± 0.56	4.23 ± 0.56	3.35 ± 0.32	3.42 ± 0.31
$\chi^2/\text{d.o.f}$	29.62/(53-8)	31.48/(53-8)	26.168/(48-8)	33.661/(48-8)

Table 1. Best-fit parameters obtained from fitting the monopole and quadrupole BOSS DR12 data using the theoretical approach described in §5. The two first columns are the parameters obtained from fitting the LOWZ-DR12 data, whereas the third and fourth columns are obtained from fitting the CMASS-DR12 data. The first and third columns are the parameters obtained when the covariance matrix is inferred from QPM mocks, whereas the second and fourth columns parameters are obtained when the covariance matrix is inferred from MD-PATCHY mocks. For all cases, the minimum scale used is $k_{\max} = 0.24 \text{ hMpc}^{-1}$ and the largest scales used are $k_{\min} = 0.02 \text{ hMpc}^{-1}$ for the monopole and $k_{\min} = 0.04 \text{ hMpc}^{-1}$ for the quadrupole. The error-bars represent 1σ deviations and have been inferred from the analysis of the likelihood function as it is described in §6.2. The cosmological parameters, $f\sigma_8$, $H(z)r_s(z_d)$ and $D_A(z)/r_s(z_d)$ are correlated, so we encourage using the multivariate Gaussian likelihood presented in §7.5.

Sample (Cov.)	LOWZ (QPM)	LOWZ (MD-PATCHY)	CMASS (QPM)	CMASS (MD-PATCHY)
$f(z_{\text{eff}})\sigma_8(z_{\text{eff}})$	0.476 ± 0.043	0.494 ± 0.045	0.434 ± 0.023	0.438 ± 0.021
$b_1\sigma_8(z_{\text{eff}})$	1.290 ± 0.016	1.283 ± 0.017	1.236 ± 0.012	1.236 ± 0.012
$b_2\sigma_8(z_{\text{eff}})$	-0.23 ± 0.95	-0.37 ± 0.60	0.38 ± 0.60	0.25 ± 0.56
A_{noise}	-0.32 ± 0.22	-0.41 ± 0.21	-0.044 ± 0.089	-0.064 ± 0.086
$\sigma_{\text{FoG}} [\text{Mpch}^{-1}]$	4.04 ± 0.61	4.27 ± 0.59	3.41 ± 0.31	3.45 ± 0.30
$\chi^2/\text{d.o.f}$	33.45/(53-6)	36.08/(53-6)	26.96/(48-6)	33.99/(48-6)

Table 2. Best-fit parameters obtained from fitting the monopole and quadrupole BOSS DR12 data as it has been described in Table 2, where in this case the AP parameters, $D_A(z)/r_s(z_d)$ and $H(z)r_s(z_d)$ have been set to their fiducial value, $H(z_{\text{lowz}})r_s(z_d) = 11.773 \text{ kms}^{-1}$, $D_A(z_{\text{lowz}})/r_s(z_d) = 6.7466$, $H(z_{\text{cmass}})r_s(z_d) = 13.663 \cdot 10^3 \text{ kms}^{-1}$, $D_A(z_{\text{lowz}})/r_s(z_d) = 9.4418$.

different fiducial models for Ω_m and we will discuss how this tension changes. So far we can say that the LOWZ sample data has a preference for low values of $f\sigma_8$ and α_\perp (which is translated into low values of $D_A(z)/r_s(z_d)$, according to the definitions in §5.3), which is within 1 and 2σ of the fiducial values when GR is assumed. Both parameters are correlated as we will show in §7.5, so when α_\perp is fixed to its fiducial value, $f\sigma_8$ is automatically shifted towards a solution which, in this case, is consistent with *Planck15*+GR within 1σ .

From the right panels of Fig. 9 we see that the values of AP parameters are both consistent with their fiducial values within 1σ for all k_{\max} , suggesting that there is no strong tension between the fiducial cosmology and the actual. Also, the inferred $f\sigma_8$ value when the full AP test is performed, is consistent with *Planck15*+GR within 1σ . By setting the AP parameters to their fiducial values, we do not observe any significant change on the $f\sigma_8$ parameter, besides a reduction of the error-bars, which increase the tension with *Planck15*+GR by up to 2σ .

In Table 3 we present the final measurements of this paper. They have been obtained by averaging the results presented in §4 (Table 1 and 2) using the QPM and MD-PATCHY covariances. We show the results for both the LOWZ and CMASS sample where the NGC and SGC have been combined into a single measurement. The main result of this paper is $f(0.57)\sigma_8(0.57) = 0.448 \pm 0.038$ for the CMASS and $f(0.32)\sigma_8(0.32) = 0.402 \pm 0.060$ for the LOWZ sample when the AP test is performed; and $f(0.57)\sigma_8(0.57) = 0.438 \pm 0.022$ for the CMASS and $f(0.32)\sigma_8(0.32) = 0.497 \pm 0.0436$ for the LOWZ sample then the AP parameters have been tuned to their fiducial value. In the following subsections we analyse how these results are affected by a change in the cosmological models (§7.1), how these results compares with other values of $f(z)\sigma_8(z)$ extracted from papers based on the Data Release 11 of the BOSS sample (§7.3), and how these results compare to other values of $f(z)\sigma_8(z)$ obtained from other redshift surveys (§7.4). We also present the multivariate likelihood surface at $f\sigma_8$, $H(z)r_s(z_d)$ and $D_A(z)/r_s(z_d)$ (§7.5).

7.1 Dependence with cosmology

In this section we study how sensitive the measurements of α_\perp , α_\parallel and $f\sigma_8$ are respect to the assumed cosmology for converting redshifts into comoving distances. In order to test this effect we have measured the galaxy power spectrum multipoles of the data assuming two additional cosmological models, one with $\Omega_m = 0.292$ and another with $\Omega_m = 0.332$ (see table 4 of Gil-Marín et al. 2015a for details about these two extra cosmologies, listed as H-Planck13 and L-Planck13). These two values of Ω_m are at 1σ tension of the best-fit value reported by Planck Collaboration et al. (2014). Our power spectrum models are as described in §5, but based on the linear power spectrum of the assumed cosmological model (see fig. 6 in Gil-Marín et al. 2015a for a comparison between these linear dark matter power spectra). In order to be consistent, we have re-analysed the MD-PATCHY mocks assuming the new value of Ω_m for converting redshifts into comoving distances, in order to recompute a new covariance matrix, consistent with the new measurement of the monopole and quadrupole. In Fig. 10 we show the values of α_\perp , α_\parallel and $f\sigma_8$ obtained as a function of the chosen

value for Ω_m for the LOWZ and CMASS sample in the left and right panels, respectively, using the corresponding MD-PATCHY covariance. The red, blue and green points show the results of assuming $\Omega_m = 0.292, 0.310, 0.332$, respectively. The filled symbols represent the results when the full AP test is performed, whereas the empty symbols represent the values $f\sigma_8$ obtained when the AP parameters have been set to their fiducial value (in this case α_\parallel and α_\perp are set to 1). In the bottom sub-panel panel, the dotted horizontal coloured lines show the corresponding value of $f\sigma_8$ when GR is assumed and the value of σ_8 is set to 0.815 (which is the fiducial value for the *Planck15* cosmology). In the α_\perp and α_\parallel panels, the horizontal black dotted line represent the fiducial value $\alpha_\perp = \alpha_\parallel = 1$.

For the CMASS sample, the results do not strongly depend on the fiducial cosmology chosen. For both AP and non-AP cases, the changes in $f\sigma_8$ as a function of the cosmological model assumed are typically of $\sim 0.5\sigma$. Furthermore, when the $\Omega_m = 0.31$ model is assumed, the tension between the observed $f\sigma_8$ and its *Planck15*+GR prediction minimises. Therefore, CMASS data suggests that when GR is assumed as a theory of gravity, $\Omega_m = 0.31$ is the most likely model among those studied. Also, for this case the AP parameters are the closest to the fiducial values.

For the LOWZ sample, when the AP test is performed we observe a $\sim 2\sigma$ tension for $\Omega_m^{\text{fid}} = 0.293$ and 0.310 on $f\sigma_8$. The tension is even higher when $\Omega_m^{\text{fid}} = 0.332$. Similar findings apply to the best-fit values of α_\perp parameter, whereas the best-fit value for α_\parallel is similar for the 3 studied models. When the AP test is turned off, and consequently α_\parallel and α_\perp are set to their fiducial values, we observe that the $f\sigma_8$ tension is reduced to well within 1σ for all models studied. This suggests, that the cause of the $f\sigma_8$ tension observed in Fig. 9 cannot be explained by the choice of Ω_m^{fid} . Thus, according to LOWZ data, the observed $D_A(z)/r_s(z_d)$ parameter is in $\leq 2\sigma$ tension with its fiducial value, which induces a $\leq 2\sigma$ tension in the observed $f\sigma_8$ compared to its *Planck15*+GR prediction, due to the correlation between parameters. This tension is relaxed when $D_A(z)/r_s(z_d)$ is set to its fiducial value. In any case, the $\Omega_m = 0.31$ model is the choice that presents less tension between the observed $f\sigma_8$ and its *Planck15*+GR prediction.

Overall, we conclude that both CMASS and LOWZ galaxies data is in agreement with the fiducial model $\Omega_m^{\text{fid}} = 0.31$ consistent with *Planck15* data: for the CMASS sample the tension is below 1σ and for the LOWZ sample within 2σ . For both samples, $\Omega_m^{\text{fid}} = 0.31$ is the model that minimises the tension between the observed $f\sigma_8$ and the predicted by *Planck15*+GR.

7.2 Comparison of $f\sigma_8$ with other DR11 BOSS Data Releases analyses

In this section we compare our results on $f\sigma_8$ with other studies of RSD based on the previous Data Release 11 (DR11) of the BOSS sample. DR11 contains $\sim 10\%$ less galaxies than DR12, however, we expect that this change is not sufficiently large for producing significant changes (other than systematics) in the obtained best-fit of $f\sigma_8$. In Fig. 11 we show the measurements of $f\sigma_8$ based on the following DR11 works: (Chuang et al. 2013; Beutler et al. 2014;

	LOWZ	CMASS	LOWZ (no-AP)	CMASS (no-AP)
$f(z_{\text{eff}})\sigma_8(z_{\text{eff}})$	0.394 ± 0.062	0.444 ± 0.038	0.485 ± 0.044	0.436 ± 0.022
$H(z_{\text{eff}})r_s(z_d) [10^3 \text{kms}^{-1}]$	11.41 ± 0.56	13.92 ± 0.44	11.773	13.663
$D_A(z)/r_s(z_d)$	6.35 ± 0.19	9.42 ± 0.15	6.7466	9.4418
$\alpha_{\parallel}(z_{\text{eff}})$	1.032 ± 0.053	0.982 ± 0.031	1	1
$\alpha_{\perp}(z_{\text{eff}})$	0.942 ± 0.027	0.998 ± 0.016	1	1
$b_1\sigma_8(z_{\text{eff}})$	1.281 ± 0.035	1.222 ± 0.021	1.287 ± 0.017	1.236 ± 0.012
$b_2\sigma_8(z_{\text{eff}})$	-0.29 ± 0.50	0.53 ± 0.70	-0.30 ± 0.78	0.32 ± 0.58
A_{noise}	-0.36 ± 0.22	-0.049 ± 0.086	-0.36 ± 0.22	-0.054 ± 0.077
$\sigma_{\text{FoG}} [\text{Mpch}^{-1}]$	4.08 ± 0.56	3.39 ± 0.32	4.16 ± 0.60	3.43 ± 0.31

Table 3. Combined best-fit parameters for the LOWZ- and CMASS-DR12 samples. The first column display the LOWZ results; the second column display the CMASS results; in both cases the AP test is performed. The third and fourth column display the results for LOWZ and CMASS, respectively, when no-AP test is performed. The combination has been performed taking the average of the best-fit values of parameters obtained when the covariance matrix is extracted from either QPM and MD-PATCHY mocks, as it has been listed in Tables 1 (when AP test is performed) and 2 (when no-AP test is performed). The displayed errors are also taken as the average as the ones listed in Tables 1 and 2. The minimum scale for the fit is $k_{\text{max}} = 0.24 h\text{Mpc}^{-1}$, and the large scale cuts are $k_{\text{min}} = 0.02 h\text{Mpc}^{-1}$ for the monopole and $k_{\text{min}} = 0.04 h\text{Mpc}^{-1}$ for the quadrupole.

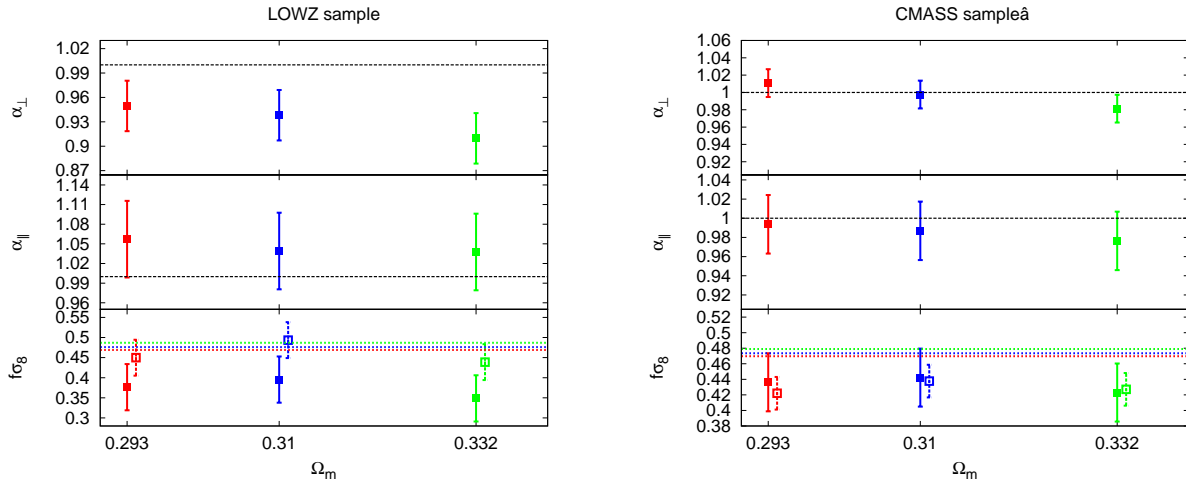


Figure 10. The left and right panels show the best-fit α_{\perp} (top sub-panel), α_{\parallel} (middle sub-panel) and $f\sigma_8$ (bottom sub-panel) value for LOWZ and CMASS sample, respectively, as a function of the chosen cosmological model to convert redshift into distances. The different colours show 3 different models, $\Omega_m = 0.293$ (red), $\Omega_m = 0.31$ (blue) and $\Omega_m = 0.332$ (green). The filled squares show the results when the AP parameters are varied, whereas for the empty squares the AP parameters have been set to their fiducial values. In the bottom sub-panel, the horizontal dashed lines show the $f\sigma_8$ prediction assuming GR ($f(z) = \Omega_m(z)^\gamma$, with $\gamma = 0.545$) and $\sigma_8 = 0.815$.

Samushia et al. 2014; Sánchez et al. 2014; Reid et al. 2014; Alam et al. 2015b; Gil-Marín et al. 2015a).

(i) Chuang et al. (2013) analyse the DR11 LOWZ and CMASS two-point correlation function monopole and quadrupole in configuration space in the range of $56 \text{Mpch}^{-1} \leq r \leq 200 \text{Mpch}^{-1}$ for CMASS and $32 \text{Mpch}^{-1} \leq r \leq 200 \text{Mpch}^{-1}$ for LOWZ. Their work include $f\sigma_8$ measurements for both LOWZ and CMASS when the AP parameters are varied, $f(0.57)\sigma_8(0.57) = 0.354 \pm 0.059$ and $f(0.32)\sigma_8(0.32) = 0.384 \pm 0.095$.

(ii) Beutler et al. (2014) compute the DR11 CMASS power spectrum monopole and quadrupole in k -space in the range of $0.01 h\text{Mpc}^{-1} \leq k \leq 0.20 h\text{Mpc}^{-1}$. They report $f(0.57)\sigma_8(0.57) = 0.419 \pm 0.044$ for the CMASS sample varying the AP parameters as well.

(iii) Samushia et al. (2014) compute the DR11 CMASS two-point correlation function monopole and quadrupole

in configuration space in the range of $24 \text{Mpch}^{-1} \leq r \leq 152 \text{Mpch}^{-1}$. When they analyse the CMASS sample they obtain $f(0.57)\sigma_8(0.57) = 0.441 \pm 0.044$ when the AP test is performed, and $f(0.57)\sigma_8(0.57) = 0.447 \pm 0.028$ when the AP parameters are tuned to their fiducial value.

(iv) Sánchez et al. (2014) analyse the two-point correlation function and the clustering wedges, parallel and perpendicular, for the DR11 LOWZ and CMASS sample using scales of $40 \text{Mpch}^{-1} \leq r \leq 180 \text{Mpch}^{-1}$ with AP test. They report $f(0.57)\sigma_8(0.57) = 0.417 \pm 0.045$ and $f(0.32)\sigma_8(0.32) = 0.48 \pm 0.10$.

(v) Reid et al. (2014) perform a small scale analysis in the range $0.8 \text{Mpch}^{-1} \leq r \leq 32 \text{Mpch}^{-1}$ using halo occupation distribution and Planck cosmology. They report $f(0.57)\sigma_8(0.57) = 0.452 \pm 0.011$ for the CMASS sample. Note that the errors on this measurements are considerably smaller, but at the same time, they rely in significant mod-

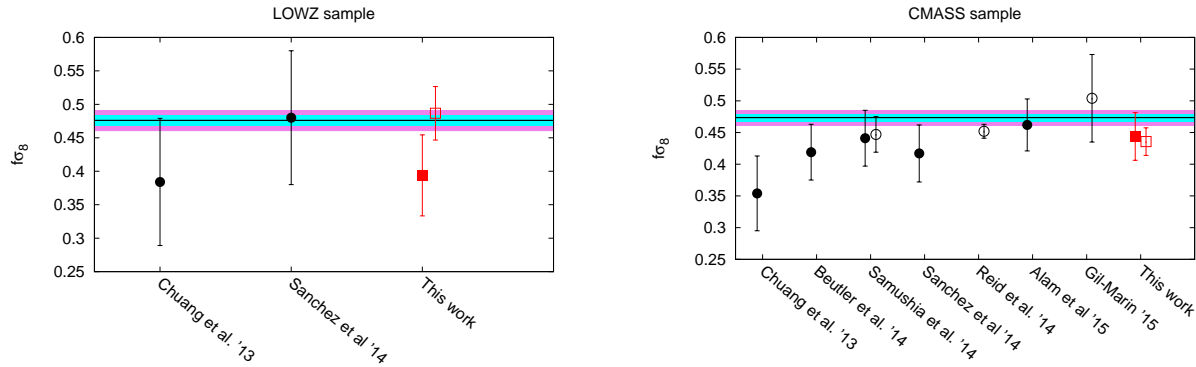


Figure 11. The constrains on $f\sigma_8$ from LOWZ- (left panel) and CMASS-DR11 samples (right panel) are displayed in black circles (Chuang et al. 2013; Beutler et al. 2014; Samushia et al. 2014; Sánchez et al. 2014; Reid et al. 2014; Alam et al. 2015b; Gil-Marín et al. 2015a). In red squares the predictions LOWZ and CMASS-DR12 samples, respectively, as they are listed in Table 3. Empty symbols are analysis with no-AP test, whereas filled symbols represents analysis where AP-test is performed. The cyan and magenta bands show the 1 and 2σ -range, respectively, allowed by Planck TT+lowP+lensing in the base Λ CDM+GR model (Planck Collaboration et al. 2015).

elling and cosmological assumptions, such as tuning the AP parameters to their fiducial value.

(vi) Alam et al. (2015b) compute the DR11 CMASS two-point correlation function monopole and quadrupole in configuration space in the range of $30 \text{ Mpc} h^{-1} \leq r \leq 126 \text{ Mpc} h^{-1}$. Their analysis includes AP results and report $f(0.57)\sigma_8(0.57) = 0.462 \pm 0.041$ for the CMASS sample.

(vii) Gil-Marín et al. (2015a) compute the DR11 CMASS power spectrum monopole and bispectrum monopole in the range of $0.03 \text{ hMpc}^{-1} \leq k \leq 0.17 \text{ hMpc}^{-1}$. They report a value of $f^{0.43}(0.57)\sigma_8(0.57) = 0.582 \pm 0.084$ using RSD and no AP effect⁴. When this value is combined with $f^{\text{Planck13}} = 0.777$ (where *Planck13* is the fiducial cosmology used in that paper; see table 4 of Gil-Marín et al. 2015a), a $f\sigma_8$ value can be obtained, $f(0.57)\sigma_8(0.57) = 0.504 \pm 0.069$. Note that this measurement is not based on the power spectrum quadrupole and relies on different cosmological assumptions.

The observed differences between the DR11 results are expected to be due to different systematics in the different models, scales and statistics considered to describe the shape of the power spectrum or two-point correlation function. With the exception of Chuang et al. (2013) in CMASS, all the results are consistent within 1 and 2σ . All the results that perform an AP analysis have a well similar error-bars.

For the CMASS sample, our $f\sigma_8$ measurement is consistent within 1σ with the DR11 reported values, with the exception of Chuang et al. (2013), which is 1.5σ below our findings and $\sim 2\sigma$ below *Planck15* prediction. In particular, our results are very close to those by Samushia et al. (2014) and Alam et al. (2015b), which are also consistent with *Planck15* data within 1σ . When the AP parameters are tuned to their fiducial value, our result on $f\sigma_8$ is also

very close to that of Samushia et al. (2014) and consistent within 1σ to the Reid et al. (2014) results.

For the LOWZ sample our result lies between the best-fit values of Chuang et al. (2013) and Sánchez et al. (2014).

7.3 Comparison of the geometrical AP parameters with other DR12 BOSS Data Releases analyses

In this section we compare our results on the geometrical AP parameters, $H(z)r_s(z_d)$ and $D_A(z)/r_s(z_d)$ with other studies based on the analysis of the anisotropic 2-point function statistics of the Data Release 12 (DR12) of the BOSS sample.

In Table 4 we compare the results from this paper (RSD-PS) with the BAO-based analysis of the anisotropic power spectrum (BAO-PS) by Gil-Marín et al. (2015b) and the BAO analysis of the anisotropic correlation function (BAO-CF) by Cuesta et al. (2015). The BAO analyses provide results based on the same dataset used by the RSD analysis, which we refer to as pre-reconstruction analyses (Pre-BAO), and on the dataset obtained after applying the reconstruction algorithm, which we refer as post-reconstruction analyses (Post-BAO).

The results of the pre-reconstruction analyses, Pre-BAO-PS, Pre-BAO-CF and RSD-PS, are very consistent with each other for both LOWZ and CMASS samples, and for both $H(z)r_s(z_d)$ and $D_A(z)/r_s(z_d)$. For LOWZ, $H(z)r_s(z_d)$ is almost exactly the same for Pre-BAO-PS, Pre-BAO-CF and RSD-PS, and $D_A(z)/r_s(z_d)$ Pre-BAO-PS and RSD-PS are $< 0.5\sigma$ apart. For CMASS, $H(z)r_s(z_d)$, there is $< 0.5\sigma$ between RSD-PS and Pre-BAO results, and the $D_A(z)/r_s(z_d)$ result is also very consistent, being the same for RSD-PS and Pre-BAO-PS, and very similar with Pre-BAO-CF as well ($< 0.5\sigma$). In general, the small differences observed between Pre-BAO-CF and Pre-BAO-PS could come from i) observational systematics (such as photometric calibration, systematic and fibre collision weights)

⁴ The quantity constrained by the power spectrum monopole in combination with the bispectrum monopole is not f times σ_8 , but f to the power 0.43 times σ_8 . For a more detailed discussion about this topic see Gil-Marín et al. (2015a)

Sample	Method-Statistic	$H(z)r_s(z_d)$	$D_A(z)/r_s(z_d)$
LOWZ	Post-BAO-PS	11.64 ± 0.62	6.85 ± 0.17
	Post-BAO-CF	11.65 ± 0.84	6.67 ± 0.13
	Pre-BAO-PS	11.44 ± 0.75	6.48 ± 0.27
	Pre-BAO-CF	11.44 ± 0.74	6.40 ± 0.37
	RSD-PS	11.41 ± 0.56	6.35 ± 0.19
CMASS	Post-BAO-PS	14.56 ± 0.38	9.42 ± 0.13
	Post-BAO-CF	14.75 ± 0.54	9.52 ± 0.14
	Pre-BAO-PS	14.10 ± 0.65	9.42 ± 0.22
	Pre-BAO-CF	14.14 ± 0.71	9.51 ± 0.19
	RSD-PS	13.92 ± 0.44	9.42 ± 0.15

Table 4. Geometrical AP parameters for LOWZ and CMASS samples: $H(z)r_s(z_d)$ (in 10^3 km s^{-1} units), $D_A(z)/r_s(z_d)$, inferred from the BAO power spectrum analysis (BAO-PS) (Gil-Marín et al. 2015b), BAO correlation function analysis (BAO-CF) (Cuesta et al. 2015), and the RSD power spectrum analysis (RSD-PS) (this work). For the BAO analyses we present the pre- and post-reconstruction results, Pre-BAO and Post-BAO, respectively. Note that the RSD results are essentially a pre-reconstruction analysis, since the RSD signal is removed in the reconstruction process.

that may affect differently the measurement of the correlation function and the power spectrum, ii) from the fact that the correlation function and power spectrum (in finite scale-ranges) do not contain exactly the same information, or iii) simply that the statistical noise affects the measurements differently in the same way as a different binning of the data. The differences between Pre-BAO-PS and RSD-PS could have their origin in systematics of the model itself, or observational systematics that enter differently in the BAO and RSD modelling. In any case, these systematics are smaller than 0.5σ .

On the other hand, the results between post-reconstruction analyses and pre-reconstruction (including RSD-PS) are more significant, but always less than 2σ . Reconstruction is known to reduce non-linear effects on the BAO signal, and some of the discrepancy could be due to this. This is discussed in more detail in both Cuesta et al. (2015); Gil-Marín et al. (2015b). For this reason, we recommend using the post-reconstruction results of $D_A(z)/r_s(z_d)$ and $H(z)r_s(z_d)$, either from Post-BAO-CF, Post-BAO-PS, or the consensus value between both results presented in both papers, for constraining cosmological models. In case also the value of $f\sigma_8$ is wanted to be used (in combination with the geometrical AP parameters) for constraining cosmological models, this paper is, at present, date the only BOSS DR12 paper that provides these measurements for the CMASS and LOWZ samples.

7.4 Comparison with other galaxy surveys

In this section we compare our measurement on $f\sigma_8$ for the LOWZ and CMASS samples with the reported $f\sigma_8$ values of other galaxy surveys at different redshifts, and with *Planck15* predictions.

Fig. 12 displays the different RSD analyses of redshift galaxy surveys. The analyses with filled symbols solve simultaneously the RSD and AP effect, whereas those represented with empty symbols only consider RSD, keeping the cosmology fixed.

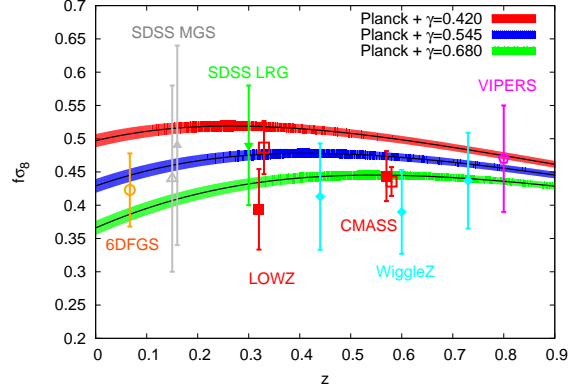


Figure 12. Constraints on $f\sigma_8$ from several redshift surveys in the base of Λ CDM, with $f(z) = \Omega_m(z)^\gamma$: orange circle (6dFGRS by Beutler et al. (2012)); gray triangle (SDSS Main Galaxy Sample by Howlett et al. (2015)); green inverse triangle (SDSS Luminous Red Galaxies by Oka et al. (2014)); cyan diamonds (WigglyZ by Blake et al. (2012)); and purple pentagon (VIPERS by de la Torre et al. (2013)). In red squares the results from BOSS-DR12 for the LOWZ and CMASS sample according to Table 3. Filled symbols represent the $f\sigma_8$ measurement when the RSD and the AP effect is considered, and filled symbols when only RSD effect is considered. For the empty red squares the z -position has been slightly displaced for clarity. The red, blue and green bands show the 1σ -range allowed by Planck TT+lowP+lensing in the base Λ CDM model (Planck Collaboration et al. 2015) when $\gamma = 0.420$, $\gamma = 0.545$ (GR) and $\gamma = 0.680$, respectively.

(i) The 6dFGRS survey analysis by Beutler et al. (2012) reports a value of $f(0.067)\sigma_8(0.067) = 0.423 \pm 0.055$. Their computation is based on measuring the redshift space correlation function in 2D. Since the effective redshift is very low, their measurement is insensitive to the AP effect.

(ii) The Sloan Digital Sky Survey (SDSS) Data Release 7 Main Galaxy Sample analysis by Howlett et al. (2015) reports the measurement of the two-point correlation function. Using only RSD effect they obtain $f(0.15)\sigma_8(0.15) = 0.44^{+0.16}_{-0.12}$. When the AP effect is included⁵ they obtain $f(0.15)\sigma_8(0.15) = 0.49^{+0.15}_{-0.14}$.

(iii) The analysis of the Luminous Red Galaxy (LRG) sample in the Data Release 7 of the Sloan Digital Sky Survey II by Oka et al. (2014) measures the galaxy monopole, quadrupole and hexadecapole power spectrum multipoles. They use the RSD and AP effect to report $f(0.3)\sigma_8(0.3) = 0.49 \pm 0.09$.

(iv) The WigglyZ analysis by Blake et al. (2012) measures the galaxy correlation function and power spectrum. Considering both RSD and AP effects, they report $f\sigma_8$ at 3 different redshifts, $f(0.44)\sigma_8(0.44) = 0.413 \pm 0.080$, $f(0.6)\sigma_8(0.6) = 0.390 \pm 0.063$ and $f(0.73)\sigma_8(0.73) = 0.437 \pm 0.072$.

(v) The analysis of VIPERS by de la Torre et al. (2013)

⁵ In this result the AP effect is only partially included since α_{\parallel} and α_{\perp} are set to be equal but freely vary. When both parameters are set free the reported value is $f\sigma_8 = 0.63^{+0.24}_{-0.27}$.

measures the two-point correlation function. Using the RSD effect they report $f(0.8)\sigma_8(0.8) = 0.47 \pm 0.08$. Given the volume of the survey, the results are very insensitive to the AP effect, which is not taken into account.

In Fig. 12 we also plot the model predictions for *Planck15* best-fit, $\Omega_m = 0.308$, when different theories of gravity are assumed. We work on the assumption of $f = \Omega_m(z)^\gamma$. The prediction for GR with a cosmological constant is $\gamma = 0.545$, which is plotted in blue bands (the 1σ limits). We also plot the predictions for two additional values of γ , in red bands we plot $\gamma = 0.420$ and in green bands $\gamma = 0.680$.

Under the assumption of *Planck15*+GR, the γ factor depends on the dark energy equation of state, ω . For $\omega = -1$ we have the cosmological constant prediction, $\gamma = 0.545$. We observe that in general all the results are in agreement with this prediction within 1σ and 2σ confidence levels. For dark energy models with $\omega > -1$, such as the parametrised Post-Friedman scalar field models, $\gamma > 0.545$; whereas for $\omega < -1$, such as phantom dark energy models, $\gamma < 0.545$. In the light of results of Fig. 12, we observe that qualitatively, redshift galaxy surveys observations slightly favour models with $\omega > -1$, if Λ CDM + GR is assumed, although the deviation with respect $\omega = -1$ is not very significant. On the other hand, if the GR condition is relaxed, γ can also change. This is the case for example of the DGP model (Dvali, Gabadadze & Porrati 2000), whose prediction for γ is 0.68, and it is slightly favoured with respect to GR.

7.5 Correlated Measurements

In this subsection we present the multivariate Gaussian likelihoods calculated from the DR12 data from which marginalised results were presented in Table 1. We focus on those parameters which are of cosmological interest, such as $f\sigma_8$, $H(z)r_s(z_d)$ and $D_A(z)/r_s(z_d)$. The errors of these parameters are highly correlated, as one can infer from Fig. 7. Therefore, to jointly use these data, one needs to use their covariance matrix.

We start by defining the data vector containing the cosmology parameters of interest $f(z)\sigma_8(z)$, $H(z)r_s(z_d)$ (in 10^3kms^{-1} units) and $D_A(z)/r_s(z_d)$,

$$D^{\text{data}}(z) = \begin{pmatrix} f(z)\sigma_8(z) \\ H(z)r_s(z_d) [10^3 \text{kms}^{-1}] \\ D_A(z)/r_s(z_d) \end{pmatrix}. \quad (19)$$

The best-fit values of the LOWZ and CMASS samples for these parameters are presented in Table 1, given a covariance matrix, either QPM or MD-PATCHY.

The covariance matrices of these parameters are,

$$C_{\text{LOWZ}}^{\text{MD-PATCHY}} = 10^{-3} \begin{pmatrix} 4.1028 & 25.549 & 7.4600 \\ - & 310.08 & 51.366 \\ - & - & 34.912 \end{pmatrix}, \quad (20)$$

$$C_{\text{LOWZ}}^{\text{QPM}} = 10^{-3} \begin{pmatrix} 3.7082 & 22.721 & 7.2898 \\ - & 301.46 & 50.403 \\ - & - & 32.718 \end{pmatrix}, \quad (21)$$

$$C_{\text{CMASS}}^{\text{MD-PATCHY}} = 10^{-3} \begin{pmatrix} 1.3424 & 10.597 & 3.7495 \\ - & 179.80 & 34.180 \\ - & - & 23.495 \end{pmatrix}, \quad (22)$$

$$C_{\text{CMASS}}^{\text{QPM}} = 10^{-3} \begin{pmatrix} 1.4475 & 11.244 & 4.0507 \\ - & 188.69 & 36.234 \\ - & - & 24.698 \end{pmatrix}, \quad (23)$$

for LOWZ and CMASS samples, using the QPM or MD-PATCHY mocks to infer the best fit parameters from the power spectrum multipoles measurements, as labeled. These covariance matrices are symmetric by construction ($C_{ij} \equiv C_{ji}$) and consequently we only provide the results of half of the matrix.

From these matrices, the likelihood of any cosmological model is given by,

$$\mathcal{L} \propto \exp \left[-(D^{\text{data}} - D^{\text{model}})^T C^{-1} (D^{\text{data}} - D^{\text{model}}) / 2 \right], \quad (24)$$

where D^{model} is the vector with the model prediction for the same cosmological parameters as D^{data} .

In Fig. 13 we show the ellipses which represent the likelihood surface of 1σ ($\Delta\chi^2 = 2.30$) and 2σ ($\Delta\chi^2 = 6.17$), corresponding to the covariance matrices presented above, for LOWZ and CMASS samples, left and right panels, respectively, for MD-PATCHY (red lines) and for QPM mocks (blue lines). Each ellipse is centered in the minimum solution presented in Table 1. We observe that the differences between the covariances are small, and most of the shifts are in the minimum where they are centered, and not in the shape and orientation of the ellipsoid itself. Therefore, we conclude that the difference in covariance obtained by using either MD-PATCHY or QPM mocks is not significant.

8 CONCLUSIONS

In this paper we have presented a measurement of the isotropic and anisotropic power spectrum relative to the LOS of the LOWZ and CMASS DR12 galaxy samples of the Baryon Oscillations Spectroscopic Survey of the Sloan Digital Sky Survey III. We have analysed the redshift space distortions in the power spectrum multipoles and the constraints imposed on the growth factor times the amplitude of linear power spectrum, $f\sigma_8$. We have also considered the geometrical Alcock-Paczynski effect, which allows us to set constraints on the angular diameter distance parameter $D_A(z_{\text{eff}})/r_s(z_d)$ and the Hubble parameter $H(z_{\text{eff}})r_s(z_d)$. We study the BAO peak position on the monopole and quadrupole power spectrum in a companion paper which is released at the same time of the present paper (Gil-Marín et al. 2015b).

In order to extract cosmological information from the galaxy power spectrum multipole measurements we have used a non-local and non-linear bias model (McDonald & Roy 2009) which depends on 4 parameters, b_1 , b_2 , b_{s2} and b_{3nl} . Imposing that the bias is local in Lagrangian space, b_{s2} and b_{3nl} are set by the value of b_1 , and therefore only two free parameters are left to marginalise over, b_1 and b_2 . To model the RSD we use the TNS model Taruya, Nishimichi & Saito (2010); Nishimichi & Taruya (2011) which has been used in previous data releases of BOSS to describe the power spectrum multipoles, as well as the bispectrum monopole. The RSD model depends on the logarithmic rate of structure growth, f , on the FoG damping parameter, σ_{FoG} and

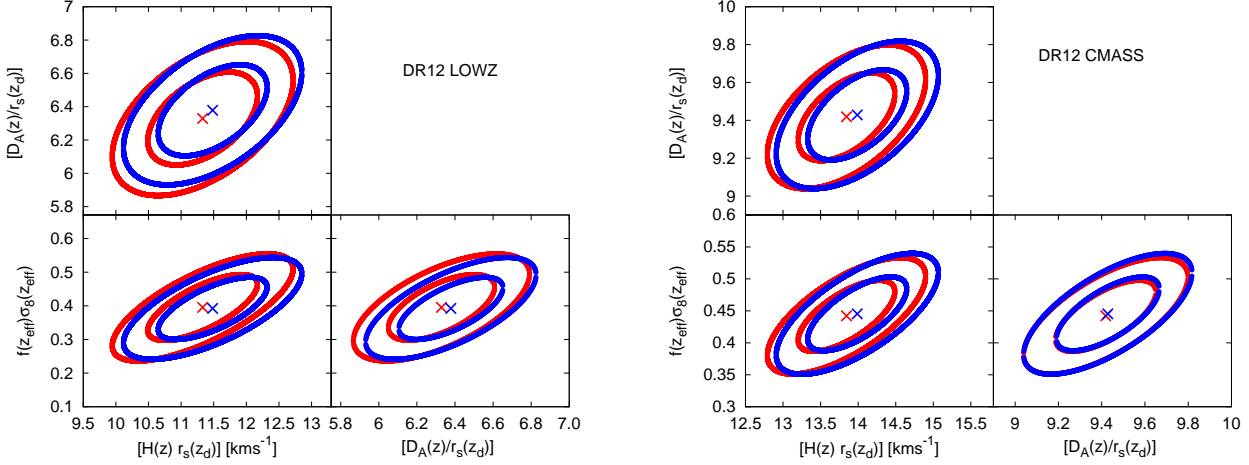


Figure 13. Likelihood surfaces of the parameters $f\sigma_8$, $D_A(z)/r_s(z_d)$ and $H(z)r_s(z_d)$ extracted from the DR12 data, LOWZ sample (left panel) and CMASS sample (right panel), using the covariance matrices provided by MD-PATCHY mocks (red ellipses) and QPM mocks (blue ellipses). Each ellipse correspond to 1σ ($\Delta\chi^2 = 2.30$) and 2σ ($\Delta\chi^2 = 6.17$) confidence levels, when the 3 parameters are marginalised. Each type of ellipse has been centered on the minimum solution presented in Table 1.

on the value of the shot noise. Although f is directly related to the assumed Ω_m given a theory of gravity, we have kept it free in order to test possible deviations from GR. In order to model the real space quantities in the TNS model, we have used the resummed perturbation theory at 2-loop order presented in Gil-Marín et al. (2012). In our model we have also included the geometrical AP effect, through the dilation parameters α_{\parallel} and α_{\perp} , which modifies the wave modes parallel and perpendicular to the LOS, respectively. These parameters are related to the angular diameter distance and the Hubble parameter, which we are also able to constrain. In our analysis we have fixed the shape of the linear power spectrum using the fiducial cosmology Ω_m^{fid} , but we have marginalised over the amplitude σ_8 . In total, our galaxy redshift space power spectrum model has 8 free parameters we marginalise over.

We have tested possible systematics of our model using the MD-PATCHY mocks simulations, which have been designed to reproduce up to $k \simeq 0.3 h\text{Mpc}^{-1}$ the power spectrum and bispectrum of data and simulations (Kitaura et al. 2015, companion paper). Using the mean from the 2048 simulations to gain signal, we find that we are able to recover $f\sigma_8$ with an accuracy of $< 3\%$ for LOWZ and $< 2\%$ for CMASS with a $k_{\text{max}} \leq 0.24 h\text{Mpc}^{-1}$. The systematics observed are significantly smaller than the statistical errors we measure for the DR12 BOSS data, and therefore we do not consider to correct the measurements, neither the corresponding errors.

We have computed the full covariance matrix of the power spectrum multipoles using two different types of galaxy mocks, 1000 realizations of QPM mocks and 2048 realizations of MD-PATCHY mocks, and we have performed two parallel analyses using these two covariance matrices. Since the differences in the best fit parameters and their corresponding errors have been found to be small, we have decided to take the average among these two approaches, to generate a unique set of results.

We find that for the DR12 LOWZ sample

$f(z_{\text{lowz}})\sigma_8(z_{\text{lowz}}) = 0.394 \pm 0.062$, $D_A(z_{\text{lowz}})/r_s(z_d) = 6.35 \pm 0.19$, $H(z_{\text{lowz}})r_s(z_d) = (11.41 \pm 0.56) 10^3 \text{kms}^{-1}$, where $z_{\text{lowz}} = 0.32$. For DR12 CMASS we find $f(z_{\text{cmass}})\sigma_8(z_{\text{cmass}}) = 0.444 \pm 0.038$, $D_A(z_{\text{cmass}})/r_s(z_d) = 9.42 \pm 0.15$, $H(z_{\text{cmass}})r_s(z_d) = (13.92 \pm 0.44) 10^3 \text{kms}^{-1}$, where $z_{\text{cmass}} = 0.57$. A covariance matrix for these measurements was also presented. These are the main results of this paper and are in general agreement with previous BOSS DR11 measurements. Furthermore, we have been able to reduce the previous error-bars on $f\sigma_8$, shrinking them down to 15% for LOWZ sample and 8.5% for CMASS sample, which are the most precise measurements of this parameter at these redshifts at the moment, when the full AP effect is considered. Additionally, if we assume that the Hubble parameter and angular distance parameter are fixed at fiducial ΛCDM values, we find $f(z_{\text{lowz}})\sigma_8(z_{\text{lowz}}) = 0.485 \pm 0.044$ and $f(z_{\text{cmass}})\sigma_8(z_{\text{cmass}}) = 0.436 \pm 0.022$ for the LOWZ and CMASS samples, respectively. In this case the error bars represent a 9.1% for LOWZ and 5.0% for CMASS.

Moreover, we have analysed the data with two additional cosmological models, $\Omega_m = 0.292$ and $\Omega_m = 0.332$, which in this case we have changed the shape of the linear power spectrum of our model, accordingly. Overall, we observe that both CMASS and LOWZ galaxies data is in agreement with the fiducial model $\Omega_m^{\text{fid}} = 0.31$ consistent with *Planck15* data: for the CMASS sample the tension is below 1σ and for the LOWZ sample within 2σ . For both samples, when the cosmological model is changed, the value of $f\sigma_8$ only changes by $\leq 0.5\sigma$.

The constraints on $f(z_{\text{eff}})\sigma_8(z_{\text{eff}})$, along with $H(z_{\text{eff}})r_d(z)$ and $D_a(z_{\text{eff}})r_d(z_{\text{eff}})$, will be useful in a joint analysis with other cosmological data sets (in particular CMB data) for setting stringent constraints on neutrino mass, dark energy, gravity, curvature as well as number of neutrino species.

ACKNOWLEDGEMENTS

HGM is grateful for support from the UK Science and Technology Facilities Council through the grant ST/I001204/1. WJP is grateful for support from the UK Science and Technology Facilities Research Council through the grant ST/I001204/1, and the European Research Council through the grant “Darksurvey”. FSK acknowledges the support of the Karl-Schwarzschild Program from the Leibniz Society. FSK, SRT, CC, and FP acknowledge support from the Spanish MICINN’s Consolider-Ingenio 2010 Programme under grant MultiDark CSD2009-00064, MINECO Centro de Excelencia Severo Ochoa Programme under grant SEV-2012-0249, and grant AYA2014-60641-C2- 1-P. The massive production of all MultiDark Patchy BOSS DR12 mocks has been performed at the BSC Marenostrum supercomputer, the Hydra cluster at the Instituto de Fisica Teorica UAM/CSIC and NERSC at the Lawrence Berkeley National Laboratory.

We thank Shun Saito and Florian Beutler for comments and helpful discussions.

Funding for SDSS-III has been provided by the Alfred P. Sloan Foundation, the Participating Institutions, the National Science Foundation, and the U.S. Department of Energy Office of Science. The SDSS-III web site is <http://www.sdss3.org/>.

SDSS-III is managed by the Astrophysical Research Consortium for the Participating Institutions of the SDSS-III Collaboration including the University of Arizona, the Brazilian Participation Group, Brookhaven National Laboratory, University of Cambridge, Carnegie Mellon University, University of Florida, the French Participation Group, the German Participation Group, Harvard University, the Instituto de Astrofísica de Canarias, the Michigan State/Notre Dame/JINA Participation Group, Johns Hopkins University, Lawrence Berkeley National Laboratory, Max Planck Institute for Astrophysics, Max Planck Institute for Extraterrestrial Physics, New Mexico State University, New York University, Ohio State University, Pennsylvania State University, University of Portsmouth, Princeton University, the Spanish Participation Group, University of Tokyo, University of Utah, Vanderbilt University, University of Virginia, University of Washington, and Yale University. This research used resources of the National Energy Research Scientific Computing Center, which is supported by the Office of Science of the U.S. Department of Energy under Contract No. DE-AC02-05CH11231.

Numerical computations were done on the Sciama High Performance Compute (HPC) cluster which is supported by the ICG, SEPNet and the University of Portsmouth.

REFERENCES

- Alam S. et al., 2015a, *ApJS*, 219, 12
 Alam S., Ho S., Vargas-Magaña M., Schneider D. P., 2015b, ArXiv e-prints
 Alcock C., Paczynski B., 1979, *Nature*, 281, 358
 Anderson L. et al., 2014, *MNRAS*, 441, 24
 Anselmi S., Pietroni M., 2012, *J. Cosmology Astropart. Phys.*, 12, 13
 Bernardeau F., Colombi S., Gaztañaga E., Scoccimarro R., 2002, *Phys. Rep.*, 367, 1
 Bernardeau F., Crocce M., Scoccimarro R., 2008, *Phys. Rev. D*, 78, 103521
 Bernardeau F., Crocce M., Scoccimarro R., 2012, *Phys. Rev. D*, 85, 123519
 Beutler F. et al., 2012, *MNRAS*, 423, 3430
 Beutler F. et al., 2014, *MNRAS*, 443, 1065
 Biagetti M., Chan K. C., Desjacques V., Paranjape A., 2014, *MNRAS*, 441, 1457
 Bianchi D., Gil-Marín H., Ruggeri R., Percival W. J., 2015, ArXiv e-prints
 Blake C. et al., 2012, *MNRAS*, 425, 405
 Bolton A. S. et al., 2012, *AJ*, 144, 144
 Carlson J., White M., Padmanabhan N., 2009, *Phys. Rev. D*, 80, 043531
 Chuang C.-H. et al., 2013, *MNRAS*, 433, 3559
 Crocce M., Scoccimarro R., 2006, *Phys. Rev. D*, 73, 063519
 Cuesta A. J. et al., 2015, ArXiv e-prints
 Dawson K. S. et al., 2013, *AJ*, 145, 10
 de la Torre S. et al., 2013, *A&A*, 557, A54
 Doi M. et al., 2010, *AJ*, 139, 1628
 Dvali G., Gabadadze G., Porrati M., 2000, *Physics Letters B*, 485, 208
 Eisenstein D. J. et al., 2011, *AJ*, 142, 72
 Elia A., Kulkarni S., Porciani C., Pietroni M., Matarrese S., 2011, *MNRAS*, 416, 1703
 Feldman H. A., Kaiser N., Peacock J. A., 1994, *ApJ*, 426, 23
 Fukugita M., Ichikawa T., Gunn J. E., Doi M., Shimasaku K., Schneider D. P., 1996, *AJ*, 111, 1748
 Gil-Marín H., Noreña J., Verde L., Percival W. J., Wagner C., Manera M., Schneider D. P., 2015a, *MNRAS*, 451, 539
 Gil-Marín H. et al., 2015b, ArXiv e-prints
 Gil-Marín H., Wagner C., Noreña J., Verde L., Percival W., 2014, *J. Cosmology Astropart. Phys.*, 12, 29
 Gil-Marín H., Wagner C., Verde L., Porciani C., Jimenez R., 2012, *J. Cosmology Astropart. Phys.*, 11, 29
 Gunn J. E. et al., 1998, *AJ*, 116, 3040
 Gunn J. E. et al., 2006, *AJ*, 131, 2332
 Hartlap J., Simon P., Schneider P., 2007, *A&A*, 464, 399
 Hawkins E. et al., 2003, *MNRAS*, 346, 78
 Hivon E., Bouchet F. R., Colombi S., Juszkiewicz R., 1995, *A&A*, 298, 643
 Howlett C., Ross A. J., Samushia L., Percival W. J., Manera M., 2015, *MNRAS*, 449, 848
 Kaiser N., 1987, *MNRAS*, 227, 1
 Kitaura F.-S., Heß S., 2013, *MNRAS*, 435, L78
 Kitaura F.-S. et al., 2015, ArXiv e-prints
 Lewis A., Challinor A., Lasenby A., 2000, *Astrophys. J.*, 538, 473
 Manera M. et al., 2013, *MNRAS*, 428, 1036
 Matsubara T., 2008, *Phys. Rev. D*, 77, 063530
 McDonald P., Roy A., 2009, *J. Cosmology Astropart. Phys.*, 8, 20
 Nishimichi T., Taruya A., 2011, *Phys. Rev. D*, 84, 043526
 Oka A., Saito S., Nishimichi T., Taruya A., Yamamoto K., 2014, *MNRAS*, 439, 2515
 Okamura T., Taruya A., Matsubara T., 2011, *J. Cosmology Astropart. Phys.*, 8, 12
 Okumura T., Seljak U., Desjacques V., 2012, *J. Cosmology Astropart. Phys.*, 11, 14
 Peacock J. A. et al., 2001, *Nature*, 410, 169
 Peacock J. A., Nicholson D., 1991, *MNRAS*, 253, 307

- Percival W. J. et al., 2004, *MNRAS*, 353, 1201
Percival W. J. et al., 2014, *MNRAS*, 439, 2531
Pietroni M., 2008, *J. Cosmology Astropart. Phys.*, 10, 36
Planck Collaboration et al., 2014, *A&A*, 571, A16
Planck Collaboration et al., 2015, ArXiv e-prints
Reid B. et al., 2015, ArXiv e-prints
Reid B. A., Seo H.-J., Leauthaud A., Tinker J. L., White M., 2014, *MNRAS*, 444, 476
Reid B. A., White M., 2011, *MNRAS*, 417, 1913
Ross A. J., et al. in prep., 000
Ross A. J. et al., 2012, *MNRAS*, 424, 564
Saito S., Baldauf T., Vlah Z., Seljak U., Okumura T., McDonald P., 2014, ArXiv e-prints
Samushia L., Branchini E., Percival W., 2015, ArXiv e-prints
Samushia L. et al., 2013, *MNRAS*, 429, 1514
Samushia L. et al., 2014, *MNRAS*, 439, 3504
Sánchez A. G. et al., 2014, *MNRAS*, 440, 2692
Smee S. A. et al., 2013, *AJ*, 146, 32
Smith J. A. et al., 2002, *AJ*, 123, 2121
Tadros H. et al., 1999, *MNRAS*, 305, 527
Taruya A., Bernardeau F., Nishimichi T., Codis S., 2012, *Phys. Rev. D*, 86, 103528
Taruya A., Hiramatsu T., 2008, *ApJ*, 674, 617
Taruya A., Nishimichi T., Saito S., 2010, *Phys. Rev. D*, 82, 063522
Valageas P., Nishimichi T., 2011, *A&A*, 527, A87
Vlah Z., Seljak U., McDonald P., Okumura T., Baldauf T., 2012, *J. Cosmology Astropart. Phys.*, 11, 9
Wang X., Szalay A., 2012, *Phys. Rev. D*, 86, 043508
White M., Tinker J. L., McBride C. K., 2014, *MNRAS*, 437, 2594
Yamamoto K., Nakamichi M., Kamino A., Bassett B. A., Nishioka H., 2006, *PASJ*, 58, 93
Yoo J., Seljak U., 2015, *MNRAS*, 447, 1789

APPENDIX A: EFFECT OF SYSTEMATIC WEIGHTS AT LARGE SCALES

In this appendix we study the impact of the systematic weights in the power spectrum monopole and quadrupole of the CMASS sample. The systematic weights are designed to correct for fluctuations in the target density caused by changes in the observational efficiency (Ross et al. in prep.). The CMASS sample presents correlations between the galaxy density at large scales and the systematic weights are designed to correct for these variations giving an isotropic weighted field. However, the accuracy of these weights is limited and we are interested in their accuracy not only for the monopole, but also for the quadrupole, which we expect to be more sensitive to these corrections.

In order to test this effect, we have analysed the CMASS data power spectrum multipoles before (pre-systematic-weight correction power spectrum, $P_{\text{no-sys}}$) and after the application of the systematic weights (post-systematic-weight correction power spectrum, P_{sys}). We expect that these pre- and post-systematic-weight power spectrum multipoles converge to the same values at sufficiently small scales, where the fluctuations in the target density are not relevant. However, at larger scales, where the effects of the fluctuations in the target density are not negligible, they will predict

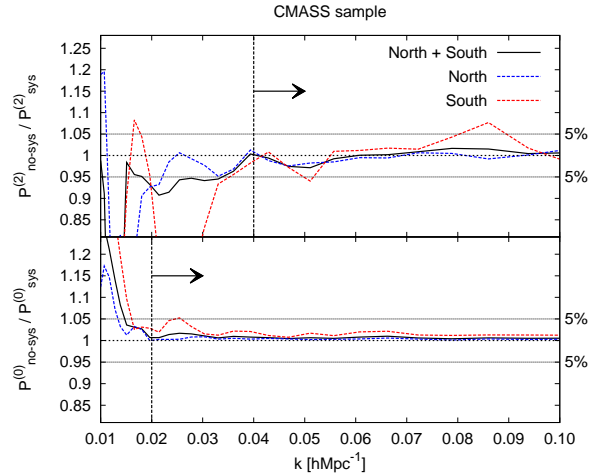


Figure A1. Effect of systematic weights in the CMASS data sample for the NGC (blue dashed lines), SGC (red dashed lines) and NGC+SGC (black solid lines). The arrows indicate the large scale cuts applied in order to keep those scales where the correction represents less than $\sim 5\%$ of the signal. These k -cuts are $k = 0.02 \text{ hMpc}^{-1}$ for the monopole (lower sub-panel) and $k = 0.04 \text{ hMpc}^{-1}$ for the quadrupole (upper sub-panel).

different power spectrum amplitudes. By analyzing this difference, we will estimate the percentile correction of the systematic weights on the power spectrum multipoles. Setting a limit of $\sim 5\%$ correction, we define a large scale cutoff for the power spectrum multipoles.

This is displayed in Fig. A1, where the ratio between the data power spectrum multipoles is shown for the monopole (lower sub-panel) and quadrupole (upper sub-panel). The different colour lines show this effect for the NGC, SGC, and NGC+SGC as labeled.

As expected, the effect of the systematic weights is relevant only at large scales, where they suppress spurious correlations and has a higher impact on the quadrupole respect to the monopole. Setting an accuracy limit of $\sim 5\%$ correction, we discard those scales where the systematic weight correction on the power spectrum multipoles exceeds this limit. Furthermore, we can compute the χ^2 for the difference between the weighted and unweighted $P^{(0)}$ and $P^{(2)}$. This is $\chi^2 = DC^{-1}D^t$, where $D \equiv P_{\text{sys}} - P_{\text{no-sys}}$. We obtain that for $k_{\text{min}} = 0.02 \text{ hMpc}^{-1}$ for the monopole and $k_{\text{min}} = 0.04 \text{ hMpc}^{-1}$ for the quadrupole, (as indicated by the black arrows) and $k_{\text{max}} = 0.25 \text{ hMpc}^{-1}$ for both statistic, the reduced χ^2 is 0.044. This means that by applying the weights we are maximally correcting by just $\sim 0.2\sigma$ ($0.2 \simeq \sqrt{0.044}$) in some measured parameter. This set a maximal impact of the known systematic without the need of defining any particular model.

Therefore, in this paper we will only consider for our analyses those scales smaller than $k = 0.02 \text{ hMpc}^{-1}$ for the monopole and $k = 0.04 \text{ hMpc}^{-1}$ in the quadrupole, as indicated by the black arrows.

	DR12 dataset	QPM	MD-PATCHY
LOWZ	0.0157	0.0418	0.0148
CMASS	0.0528	0.0529	0.0349

Table B1. Fraction of collided galaxies, $f_{cg} \equiv \sum_i [w_{fc}(\mathbf{x}_i) - 1] / \sum_i w_{fc}(\mathbf{x}_i)$, for the data, for the QPM and MD-PATCHY mocks, for the CMASS and LOWZ samples.

APPENDIX B: EFFECT OF FIBER COLLISIONS WEIGHTS ON THE BEST-FIT PARAMETER ESTIMATION

In this appendix we study the effect of the fiber collision weights on the power spectrum multipoles, and more precisely on the $f\sigma_8$ measurement according to the model presented in §5. As described in §2.1, the fiber collision weights are included in order to account for those galaxy pairs that are too close to each other ($< 62''$) to put two fibre detectors. The fraction of collided galaxies, $f_{cg} \equiv \sum_i [w_{fc}(\mathbf{x}_i) - 1] / \sum_i w_{fc}(\mathbf{x}_i)$, for the data is presented in the first column of Table B1, for the CMASS and LOWZ samples. Since the number density of galaxies is higher in the CMASS sample, the fraction of collided galaxies is also higher in this sample. The second and the third column of Table B1 present the fraction of collided galaxies found in the QPM and MD-PATCHY mocks, respectively. For the CMASS sample, the MD-PATCHY mocks present a smaller value of f_{cg} respect to the data and QPM mocks, which both are in close agreement. This is due to a limitation in the resolution of substructure inside MD-PATCHY haloes. This limitation will be solved in future versions of the MD-PATCHY mocks. In the LOWZ sample, both data and MD-PATCHY mocks agree well with the value of f_{cg} , because for the number density of galaxies of this sample, the resolution of substructure was not a limiting factor. However, we see that QPM mocks present a higher value of f_{cg} with respect to the data. This is due to the version of QPM mocks used in this paper matched an old LOWZ catalogue, where galaxies with previously known redshifts were subsample to match the BOSS close-pairs selection. This subsample has now been discontinued. As for the MD-PATCHY mocks, this will be fixed in future releases.

In order to test the effect of the fiber collisions in the parameter estimation, we focus on the QPM mocks for the CMASS sample, which has the higher value of f_{cg} amongst all the cases. We measure the monopole and quadrupole of 1000 mock realizations and take their average in order to gain signal to noise. We consider the two following selection of galaxies

(i) We treat the galaxies as in a real survey. When two or more galaxies present an angular separation of $\leq 62''$, we weight one of them by the number of galaxies within the $\leq 62''$ angular radius, and remove the others. This mimics what it is done with the real dataset

(ii) We consider all the galaxies resolved in the mocks and weight them equally. This is the ideal case we would have if all the targeted galaxies in the survey were analysed spectroscopically.

The case (ii) has the correct clustering and the correct anisotropic signal. Comparing both will show how the colli-

sion weights affect the power spectrum multipoles and the estimation of parameters.

When we compare the power spectrum monopole (and therefore the isotropic clustering) of cases (i) and (ii), we see that the effects of the collision weights are degenerate with the amplitude of the shot noise parameter, A_{noise} , which we treat as a free nuisance parameter. This was already reported in Gil-Marín et al. (2015a) for the DR11 sample using PTHALOS mocks (Manera et al. 2013). The effect of the fiber collision weights in the power spectrum quadrupole (i.e. in the anisotropic clustering) is more complex. We know that a fraction of the angular close pairs correspond to galaxies which share the same dark matter host halo. Using the regions where we have a superposition of plates, we have estimated that this fraction is about $\sim 60\%$. On the other hand, $\sim 40\%$ of the angular close pairs correspond to galaxies that happens to share a similar LOS, but that are actually reasonably uncorrelated. By applying the fiber collision weights to galaxies that are actual close pairs, we are removing signal in the direction of the LOS with respect to the signal in the transverse direction, which is not modified. Therefore, by applying the collision weights, the anisotropic power spectrum is affected, which potentially can alter the estimation of $f\sigma_8$. This is shown in the left panel of Fig. B1, where the black solid line show the fractional change in the power spectrum quadrupole of case (i) respect to case (ii), for QPM mocks. We see that this change is sub-percent at large scales, but rapidly grows as we go to smaller scales, reaching $\simeq 10\%$ at $k \simeq 0.2 h\text{Mpc}^{-1}$ and $\simeq 20\%$ at $k \simeq 0.25 h\text{Mpc}^{-1}$. In order to test the impact of this change in the fitted parameters, we fit the RSD bias model presented in §5 to the power spectrum monopole and quadrupole of cases (i) and (ii) and compare them, using the scales $0.02 h\text{Mpc}^{-1} \leq k \leq k_{\text{max}}$ for the monopole and $0.04 h\text{Mpc}^{-1} \leq k \leq k_{\text{max}}$ for the quadrupole, as we did for the data, varying k_{max} from $0.15 h\text{Mpc}^{-1}$ to $0.24 h\text{Mpc}^{-1}$. The blue dashed line of Fig. B1 shows the ratio of the best-fit models to power spectrum multipoles of cases (i) and (ii). We see that the difference among the models describes well the differences in the power spectrum quadrupole produced by the fiber collision weights. In the right panel of Fig. B1 the ratio between the best-fit parameters, $\{b_1\sigma_8, b_2\sigma_8, f\sigma_8, \sigma_{\text{FoG}}, A_{\text{noise}}, \alpha_{\parallel}, \alpha_{\perp}\}$ of these two models are shown. Both top and bottom panels display the same ratio of parameters, but at different ranges, for clarity. We observe that the change in the monopole and quadrupole due to the fiber collision weights is absorbed mainly by A_{noise} and $b_2\sigma_8$, which changes of order of $20\% - 100\%$ in the fiber collision case respect to case (i). The FoG damping parameter, σ_{FoG} changes by about 2.5% and does not present any significant change with the minimum scale of the fit. The AP parameters, α_{\parallel} and α_{\perp} do not present any significant change due to the effect of fiber collisions. Finally $f\sigma_8$ and $b_1\sigma_8$ are modified by about $\sim 0.5\%$, and show no dependence with the minimum scale of the fit. In Table B2 we summarise these results and compare them with the statistical errors for the CMASS sample using $k_{\text{max}} = 0.24 h\text{Mpc}^{-1}$.

We conclude that the effect of fiber collision are absorbed chiefly by A_{noise} and $b_2\sigma_8$. The impact of the fiber collision on $f\sigma_8$ and $b_1\sigma_8$ is a sub-percent. In this case, $f\sigma_8$ tend to be overestimated with respect to the ideal case where all the galaxies were considered, whereas $b_1\sigma_8$ tend to be un-

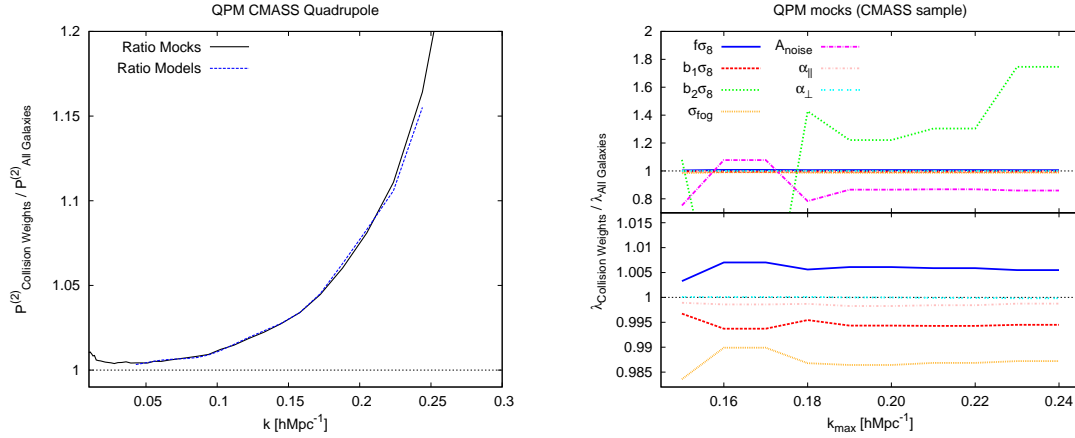


Figure B1. Effect of fiber collision weights in the CMASS sample, where the fraction of collided galaxies is 0.0529. The left panel displays the ratio between power spectrum quadrupole of the cases (i) and (ii) (see text), where the fiber collisions are applied, $P^{(2)}_{\text{CollisionWeights}}$, and where all the galaxies are considered, $P^{(2)}_{\text{AllGalaxies}}$. The black solid line is the ratio of the measured quadrupole of 1000 realizations of the QPM mocks, and the blue dashed line the ratio between the best-fit models to the cases (i) and (ii) at $k_{\text{max}} = 0.24 \text{ hMpc}^{-1}$. The right panel displays the ratio between the best-fit parameters of the best-fit models of the cases (i) and (ii). Top and bottom panel display the ratio at different scales.

Parameter	statistical error [%]	systematic error due to fc [%]
$f\sigma_8$	8.5%	0.5%
$\alpha_{ }$	3.1%	0.1%
α_{\perp}	1.6%	$\ll 0.1\%$
$b_1\sigma_8$	1.7%	0.5%
$b_2\sigma_8$	130%	70%
σ_{Fog}	9.5%	1.5%
A_{noise}	175%	10%

Table B2. Statistical and systematic errors caused by the effect of fiber collisions in the free parameters of the model, for the CMASS sample at $k_{\text{max}} = 0.24 \text{ hMpc}^{-1}$. For the cosmological parameters, $f\sigma_8$, $\alpha_{||}$ and α_{\perp} the systematic errors caused by the fiber collisions are much smaller than the statistical errors of the data for the CMASS sample.

derestimated. Finally the AP parameters present changes of order $\simeq 0.1\%$ for $\alpha_{||}$ and $\ll 0.1\%$ for α_{\perp} .

Since the 1σ statistical errors of these parameters are about 10 times larger than this systematic shift, we do not correct our result by this effect. Because the fraction of collided galaxies in the CMASS sample is higher than in the LOWZ sample, we expect that these changes are also negligible in the LOWZ sample.